UNIVERSITÀ
DEGLI STUDI
DI PADOVA

DIPARTIMENTO
DI INGEGNERIA
DELL'INFORMAZIONE

Università degli Studi di Padova
Dipartimento di Ingegneria dell'Informazione
LAUREA TRIENNALE IN INGEGNERIA DELL'INFORMAZIONE

Simulation of charged particle signals in silicon detectors with a cluster approach

Candidato:
Davide Tomasella
Matricola 1188256

Relatore:
Prof. Andrea Neviani

Correlatore:
Prof. Daniele Mengoni

ANNO ACCADEMICO 2020/2021

Preface

This thesis is the result of my stage at Legnaro National Laboratories, INFN (LNL). During this experience at LNL, I worked with GALILEO gamma-ray germanium array and EUCLIDES charged particle silicon detectors, and I started to develop the simulation program, MicroSil, subject of this thesis. After the stage, I continued to improve the MicroSil model, and analyze the simulation results till a good understanding of its key aspects.
This project gave me the opportunity to conjugate my programming attitude with my physics interests, and to employ the skills acquired during my Bachelor courses.
I wish to thank Prof. A. Neviani and Prof. D. Mengoni for the support during the development of this thesis, and the LNL GAMMA group, especially Alain and Marta, for the collaboration in the simulation design and test. I am also thankful to all professors and friends who I met during my university studies.

Davide Tomasella
Padova
Giugno 2021

Abstract

This thesis analyzes the charge collection process in silicon detectors after the interaction with a charged particle. Instead of using the standard approach with the Drift-Diffusion Model, a new approximated model is proposed to handle the high number of charges generated by heavy ions. The advantages of describing the electron and hole cloud with uniform *clusters* and the limits of this strategy are discussed thanks to implementing the model into a simulation program. The simulation is tested over different detectors and particles with particular attention to the effects of the parameters on the resulting signals. The simulated waveforms are also compared with data from Nuclear Physics experiments, i.e. EUCLIDES and FAZIA. The simulation shows a precise enough description of the detector output signals in the considered configurations.

Abstract

Questa tesi analizza il processo di raccolta delle cariche nei rivelatori al silicio dopo l'interazione di una particella carica. Invece di usare l'approccio convenzionale del modello Drift Diffusion, è stato proposto un nuovo modello approssimato per gestire la grande quantità di carica generata dagli ioni pesanti. I vantaggi di descrivere la nube di elettroni e lacune attraverso *cluster* uniformi e i suoi limiti sono discussi grazie all'implementazione del modello in un programma di simulazione. La simulazione è stata testata su diversi rivelatori e paricelle prestando particolare attenzione all'impatto dei parametri sui segnali risultanti. Le forme d'onde simulate sono state anche confrontate con dati di esperimenti di Fisica Nucleare come EUCLIDES e FAZIA. La simulazione mostra una descrizione sufficientemente accurata dei segnali dei rivelatori nelle configurazioni considerate.

Contents

1 Introduction 1

2 Charge particle detector modeling 3
2.1 Silicon detectors 3
2.1.1 Detector structure 3
2.1.2 Particle-detector interaction 5
2.1.3 Measurements 6
2.2 Charge transport in semiconductors 7
2.2.1 Drift-Diffusion Model 8
2.2.2 Commercial implementation: TCAD 11
2.3 MicroSil Model 11
2.3.1 Initial charge distribution 12
2.3.2 Clusters position evolution (charge drift) 13
2.3.3 Clusters collection 14
2.3.4 Shockley–Ramo Theorem: induced current and charge 15
2.3.5 Boundary and second-order effects (charge diffusion) 15
2.3.6 Known limits of validity 17

3 MicroSil simulation 19
3.1 Model implementation 19
3.1.1 Physics parameters (detector and particle) 19
3.1.2 Simulation initialization 21
3.1.3 ODEIV solver (Gear Method) for model evolution 21
3.1.4 FMM (Fast Multipole Method) for cluster interactions 22
3.1.5 Post-evolve operations 23
3.1.6 ROOT for graphical interface 23
3.2 Simulation setup 24
3.2.1 Configuration files generation and parameterization 24
3.2.2 Output generation and acquisition chain effects 25
3.2.3 Signal likelihood indices 25

4 Simulation results and comparison with experimental data 27
4.1 Experimental setup and collected data 27
4.1.1 EUCLIDES detectors 27
4.1.2 FAZIA dataset 28
4.2 Analysis of simulated and experimental signals 29
4.2.1 Description of the signal formation 30
4.2.2 Effects of the configuration parameters 32
4.2.3 Comparison with experimental signals 36

5 Conclusions and future developments 41

Bibliography 43

Introduction 1

This work wants to explore a different strategy in the simulation of the charge collection in silicon detectors. Such devices are tipically applied in Nuclear Physics to study the properties of charged particles with the Pulse Shape Analysis (PSA) of the detector output signals. The transport equations for semiconductors are a well-known topic and are implemented with numerical methods, i.e. Finite-Difference Methods (FDM), in several commercial programs (TCAD) that can simulate the behavior of electronic devices and circuits. Despite some of these programs can offer a large variety of tools, the energy range of the Electronics application is very different from the Nuclear Physics one where the interacting particle can generate up to 1-10 $\times 10^7$ electron-hole pairs.

The proposed approach describes the motion of the charges in the detector by approximating a group of electrons and holes with a spherical charge distribution, denominated *cluster*. Bardelli has firstly applied this concept in 2004-2006, and has created the original simulation program. I have improved Bardelli's ideas by formalizing the mathematical basis of the model and refining the simulation algorithm. I have also analyzed the simulation results with different configurations, and discussed the boundaries of this approach.

In the first Chapter *Charge particle detector modeling*, I introduced the silicon detector working principles, the particle-detector interaction, and the main steps in the detector signal acquisition. I presented the most common approach to the Transport Equations solution with the Drift-Diffusion Model (DDM) and the limits of the TCAD. I described the proposed model, the differences with the DDM, the approximations of the *cluster* approach, and its limitations.

In the second Chapter *MicroSil simulation*, I discussed the implementation of the model, the parameters, the graphical interface, and the optimization strategies adopted in the algorithm. I also presented the main aspects in the usage of the simulation and the analysis of the results.

In the third Chapter *Simulation results and comparison with experimental data*, I reported the characteristic of the detectors and read-out chain used to obtain the experimental data. I analyzed the charge collection process and the effects of key parameters in the simulated signals. Finally, I compared the experimental data with the simulated one, taking into account the acquisition system impact.

Charge particle detector modeling 2

2.1 Silicon detectors

In Particle Physics, semiconductor diode detectors, or merely solid-state detectors, are measurement devices typically used in nuclear and sub-nuclear experiments. Their high energy resolution and manufacturing are the key factors of their success. When radiation interacts in a semiconductor, electron-hole pairs are created along the path and then collected by the electrodes. The information of the incident particle or ray is, thus, translated into an electric signal and sent to the elaboration system.

2.1.1 Detector structure

The most common solid-state detectors are made from an n-Silicon bulk where a p^+-Si region creates an asymmetric p-n junction, The detector structure is displayed in Fig. 2.1. On

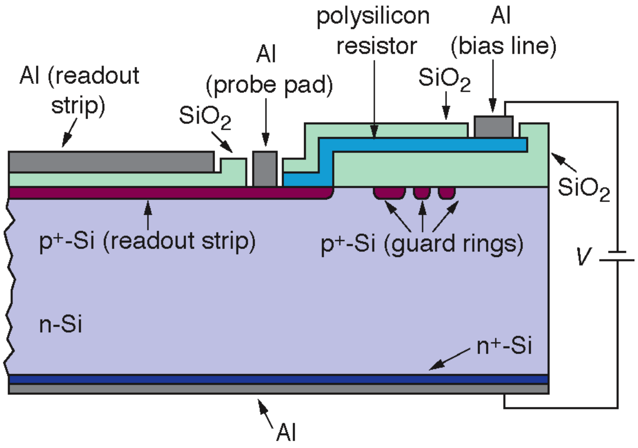
polysilicon resistor
Al (bias line)
Al (probe pad)
Al (readout strip)
SiO2
SiO2
SiO2
p+-Si (readout strip)
p+-Si (guard rings)
V
n-Si
n+-Si
Al

FIGURE 2.1: Structure of a n-Silicon detector. The silicon bulk is doped to create the n^+ and p^+ regions. The bias voltage is applied using a metal plane attached to the n^+-Si and some polysilicon resistors connected to the p^+-Si plane, strips, or pads. The SiO_2 layer isolates the readout electrodes from the semiconductive material. Image from [1].

the backside, n^+-Si is added to increase the performance of the ohmic contact. The silicon junction is used as an inverse polarized diode, usually with a reverse voltage more than the depletion one (overdepleted detectors) applied through Aluminum electrodes. Depending on the application, the thickness of the silicon can vary between 100 µm and 1 mm, and the operating voltage can commonly be within the range of 10 V to 300 V. The electrodes and the bias contacts can be shaped in strips or pads to obtain information on the particle position.
The readout electrodes or strips are commonly AC coupled with these planes to measure the amount of charge moving inside the detector. SiO_2 deposition isolates the silicon bulk and blocks the bias current leakage from the amplifier. Some polysilicon resistors, connected to the p^+-Si zones, apply the polarization voltage to the detector.
Polarizing a p-n junction through an inverse bias voltage leads to the space charge region expansion between the two doped regions (see Fig. 2.2). Since the low concentration of free charges in it, the movement of the carriers inside the depleted zone is mainly due to the electric field created by the bias electrodes that tends to pull electrons and holes out of the

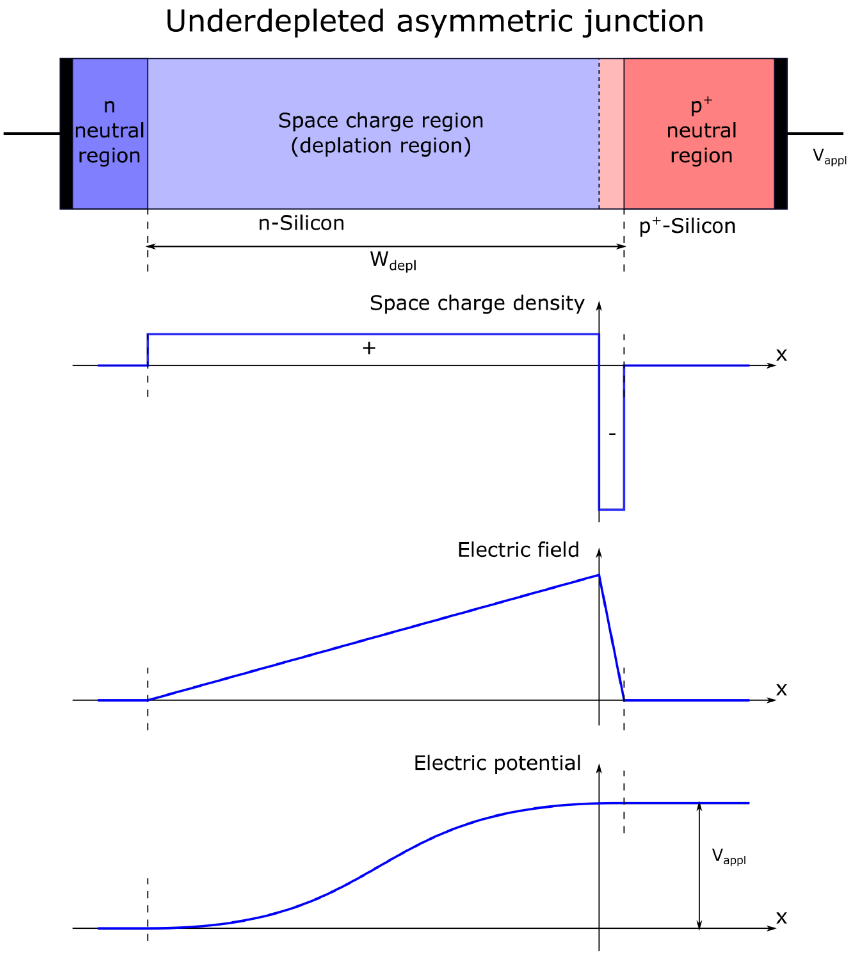
Underdepleted asymmetric junction
n neutral region
Space charge region (deplation region)
p+ neutral region
V_appl
n-Silicon
p+-Silicon
W_depl
Space charge density
+
-
x
Electric field
x
Electric potential
V_appl
x

FIGURE 2.2: A underdepleted asymmetric junction. The p^+ region is heavily doped compare to the n one, and the depletion region is more extensive in the second one to mantains the equilibrium between the two space charge regions. The high free-holes density in the p^+-Si limits the electric field penetration depth with both underdepleted and overdepleted bias voltage. The graphs show the space charge density, the electric field, and the electric potential along the junction.

depletion zone. When moving charge carriers reach the high-doped regions, the higher free charge concentration tends to diffuse them in the opposite direction, creating a dynamic equilibrium. Increasing the bias voltage over the depletion one changes this equilibrium because the concentration gradient is no large enough to stop the majority of charge motion. So a leakage current is generated, generally in the range of 10 nA to 1 µA.
Overdepleted junctions are at the base of silicon detectors because all the free charge carriers created in the n-Si are immediately collected, leaving the entire device empty of moving charges. Thus, the non-active layer decreases and, when a particle interacts with the silicon, the number of moving electron-hole pairs created is proportional to the particle energy loss.

2.1.2 Particle-detector interaction

When heavy charged particles interact in a solid-state detector, they lose energy until they exit from the material or completely stop inside it [2]. The energy loss depends on the stopping power of the material and the type of incident radiation. Bragg curves, as in Fig. 2.3, describe it. The remarkable fact is that this loss is not linear due to the different interactions happening along the particle path.

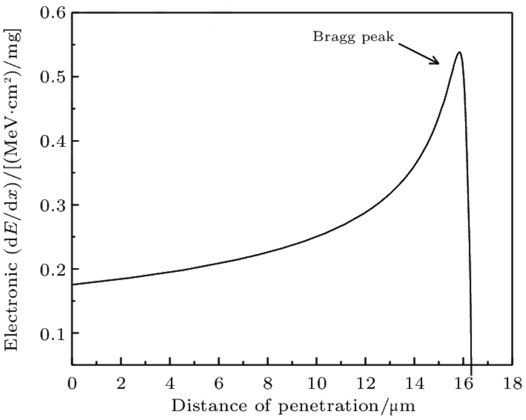

FIGURE 2.3: Bragg curve of 1.0 MeV proton penetrating Silicon. The graph shows the energy loss distribution along the particle path. The electronic and the nuclear stopping power determine the Bragg peak in the energy distribution before the ion stops in the Silicon.

When a high-energy charged particle enters a semiconductive material, it immediately interacts with the bound electrons creating an attractive Coulomb Force able to extract them from the crystal lattice. The electron-hole pairs recombination tendency is mostly suppressed in the depletion zone because no free-moving charge carriers are present. The energy transferred to the electrons leads to a decrement of the particle velocity and, when the ion is sufficiently slow, the collision with the lattice nuclei becomes more probable. The atomic nuclei receive thus enough energy to be removed from their lattice positions and generate other electron-hole pairs. If the ion stops in the material, the energy loss curve shows the characteristic Bragg peak.
The distance covered by the ion depends on initial energy and nuclear properties, i.e. mass and charge.
The electron-hole pairs, created in few picoseconds along the particle track, feel the electric field used to polarized the detector and drift in opposite directions (Fig. 2.4). This motion generates a current that persists until those carriers reach the end of the active volume.
Since in Silicon electron mobility is three times greater than hole one, the two carrier transit time may differ, and they produce two current pulses. The charge carrier initial distribution determines the time needed to collect all the ionization charges. Having a low leakage current

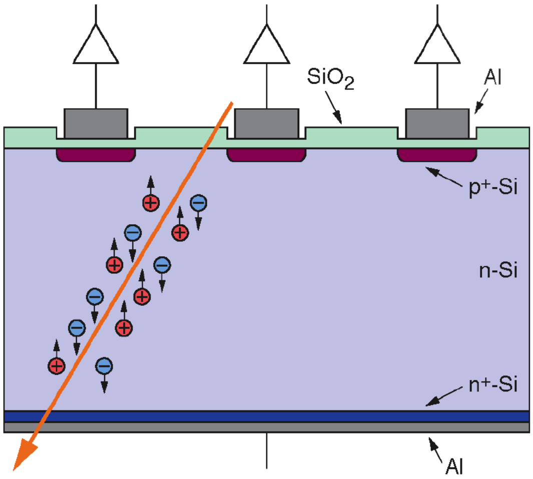

FIGURE 2.4: The incident radiation creates an electron-holes distribution along its path. In the detector active volume (depletion region) the electric field makes the carries move in opposite directions toward the collecting electrodes. The motion generates an induced current in the readout electrodes that feature the interaction. Image from [1].

is relevant to reduce the noise in the signal current, but almost impossible to archive. During its path, the high-density cloud of e^+ and h^- diffuses in the detector. The charges are collected thanks to the bias electrodes, and the junction returns to its equilibrium state. The main model describing the charge transport in a semiconductor is commonly referred as Drift-Diffusion Model.

2.1.3 Measurements

The measurement electrodes are generally connected to the p^+-Si region through some capacitors, integrated into the detector device, to eliminate the bias current contributions. The resulting signal is the induced current generated by the movement of e^+ and h^-. Shockley–Ramo Theorem determines the induced current from the initial charge distribution and the detector structure.
Considering the detector model in Fig. 2.5, the most important source of intrinsic noise in the measurement chain is the detector capacitance C [1]. The presence of the bias electrodes creates a capacitor (generally between 10 pC and 10 µC) that depends on the

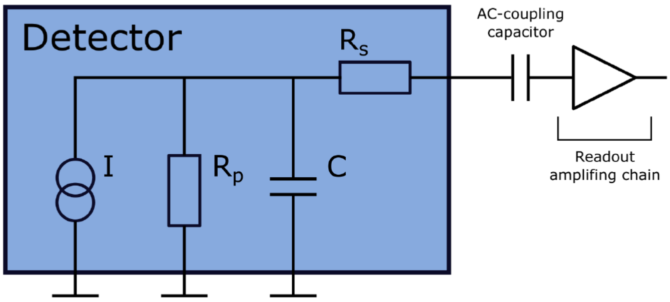

FIGURE 2.5: A detector is modeled as a noise current source. The equivalent circuit reports the main sources of noise, usually given as ENC (Equivalent Noise Charge). The readout chain is usually AC-coupled to the measurement electrodes.

detector geometry. The capacitance varies due to the bias voltage, operating temperature, and signal frequency. Using overdepleted devices reduces capacitance fluctuations. Reducing the dimensions of the detector limits the capacitance value, but this is not always possible.

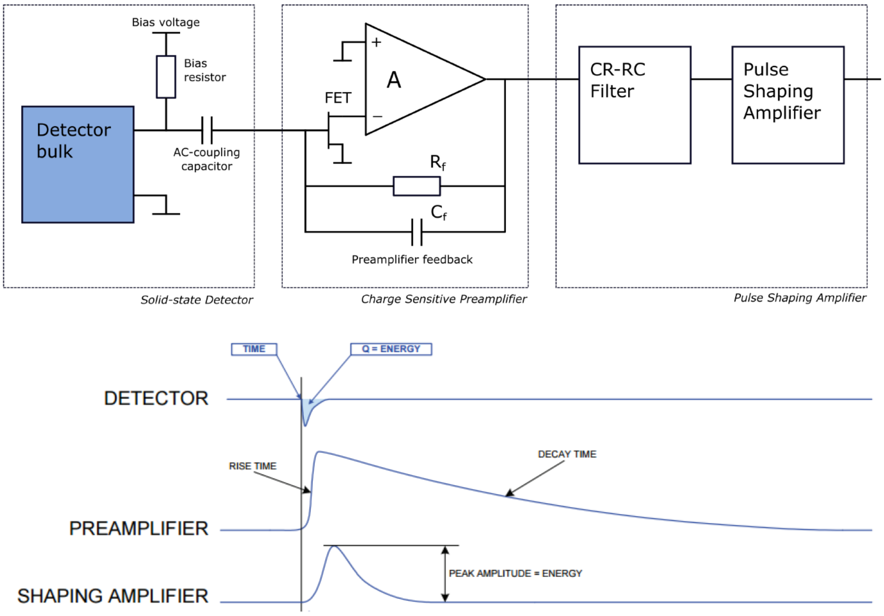
Bias voltage
Bias resistor
Detector bulk
AC-coupling capacitor
Solid-state Detector
FET
A
+
–
R_f
C_f
Preamplifier feedback
Charge Sensitive Preamplifier
CR-RC Filter
Pulse Shaping Amplifier
Pulse Shaping Amplifier
TIME
Q = ENERGY
DETECTOR
RISE TIME
DECAY TIME
PREAMPLIFIER
PEAK AMPLITUDE = ENERGY
SHAPING AMPLIFIER

FIGURE 2.6: The detector model in Fig. 2.5 is included in this simplified representation of the acquisition chain. The output signal of each stage is displayed in the lower graphs. The AC-coupling capacitor is usually integrated in the detector (see Paragraph 2.1.1). The preamplifing stage consists of a charge sensitive amplifier, commonly placed near the silicon detector to reduce external noise sources. The preamplifier output signal is usually transmitted over shielded cables to the digitizer, where the filtering and shaping stage is performed before the signal acquisition.

Readout lines connect the detector to a charge sensitive amplifier, as shown in Fig. 2.6. Those preamplifiers integrate the current impulse into a voltage pulse. An important parameter is the integration time: short time leads to high-frequency noise signals; long times increase the acquisition dead-time. Usually, after the amplification stage, the signal is filtered and then digitized. During this process, digital analysis can extract the needed information (i.e. interaction time and particle energy). Signal traces can also be saved on disk for further analysis.

2.2 Charge transport in semiconductors

The central part of the described phenomenon is the charge transport through silicon detectors. To properly simulate detector behavior is fundamental to understand the Physics law that describes this movement. The Drift-Diffusion Model (DD Model) of a semiconductor uses two transport mechanisms, denoted drift and diffusion, to describe the motion of electrons and holes. More sophisticated models have been developed: Thermodynamic Model considers the impact of temperature gradient on the charges, and Hydrodynamic Model is based on energy balance equations. Since the description of charge transport is relevant in the semiconductors industries, different commercial TCAD (Technology Computer-Aided Design) tools are used to study the silicon device behavior. Nevertheless, they are not usually designed to operate with the energy range of Nuclear Physics experiments.

2.2.1 Drift-Diffusion Model

The semiconductor equation that governs the transport of charge carriers [3] is the Poisson equation

$$\varepsilon_s \nabla \cdot \vec{E} = \rho \tag{2.1}$$

with ε_s permittivity of Si, $\vec{E}$ electric field, and ρ free charge volume density. The electric field is given by

$$\nabla \phi = \vec{E} \tag{2.2}$$

with ϕ the electric potential applied. The charge density is given by

$$\rho = -q(n - p + N_D^+ - N_A^-) \tag{2.3}$$

where q is the electron charge, n and p the free electrons and holes volume density, and N_D^+ and N_A^- concentration of acceptors and donors. From (2.1), (2.2) and (2.3) the Poisson equation is formulated as

$$\varepsilon_s \nabla^2 \phi = -q(n - p + N_D^+ - N_A^-) \tag{2.4}$$

The time-dependent current continuity equations for electrons and holes are

$$\frac{\partial n}{\partial t} = G_n - R_n + \frac{1}{q} \nabla \cdot \vec{J_n} \tag{2.5}$$

$$\frac{\partial p}{\partial t} = G_p - R_p + \frac{1}{q} \nabla \cdot \vec{J_p} \tag{2.6}$$

with $\vec{J_n}$ and $\vec{J_p}$ current densities, G_n and G_p generation rates, and R_n and R_p recombination rates.
The Drift-Diffusion Model [3] applies the Kinetic Theory of Gases to the electrons and holes cloud inside the silicon lattice. The DD Model assumes constant temperature, steady-state, and full ionization of the introduced impurities. The carrier flow is due to the externally applied electric field and the concentration gradient of charge. According to a semi-classic model, electrons and holes are particles that move through the material alternating straight-line motion with elastic collisions with the lattice ions. The average time between subsequent collisions is τ (relaxation time).

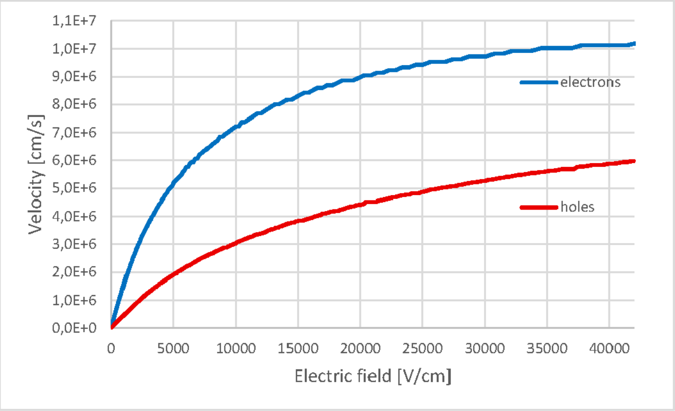

FIGURE 2.7: Electrons and holes drift velocity in silicon detectors (T=300 K). With low field the relation is linear. Increasing the electric field the velocity saturates due to the viscous friction generated by the nuclei lattice.

The drift of carriers is the effect of the electric field action and is described by the mean of the drift velocity over time $<\overline{v_d}>$. The relation between this mean velocity and the applied electric field depends on the material, the carrier mobility, and the temperature. For silicon detector application range, the relation is shown in Fig. 2.7. If the relaxation time is independent to the electric field, the equations are

$$\vec{v_d^e} = -\frac{q\tau_e}{m_e}\vec{E} \tag{2.7}$$

$$\vec{v_d^h} = -\frac{q\tau_h}{m_h}\vec{E} \tag{2.8}$$

where m_e and m_h are the effective mass of electrons and holes in silicon. Therefore, the drift current density becomes

$$\vec{J}_{n,drift} = -qn < \vec{v_d^e} >= qn\mu_n\vec{E} \tag{2.9}$$

$$\vec{J}_{p,drift} = -qp < \vec{v_d^h} >= qp\mu_p\vec{E} \tag{2.10}$$

where μ_n and μ_p are the electrons and holes mobility, and they depend on the total doping concentration $N_T = N_D^+ + N_A^-$ (see Fig. 2.8).

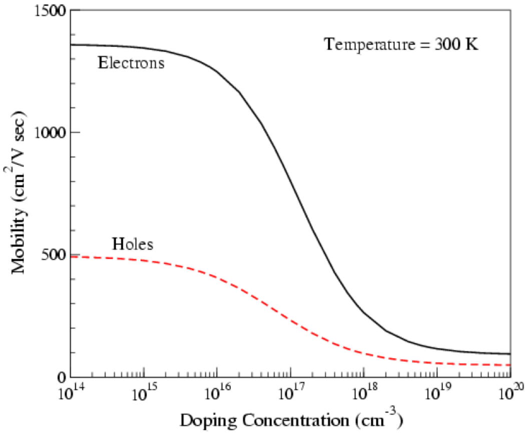

FIGURE 2.8: Electrons and holes mobility factor (T=300 K). The carrier mobility depends on the total doping concentration. With normal doping concentration (less than 10^{17}-10^{18} cm^{-3}, the electron mobility is usually consider three times greater than the hole one.

The diffusion current is due to the charge carriers that diffuse, according to the free charge density gradient, from the higher density zone to the lower one. The diffusion is an effect of the thermal agitation of electrons and holes. Fick Law determines the diffusion current density

$$\vec{J}_{n,diff} = qD_n\nabla n \tag{2.11}$$

$$\vec{J}_{p,diff} = -qD_p\nabla p \tag{2.12}$$

with D_n and D_p diffusion coefficients, reported in Fig. 2.9.
Einstein relation shows the dependence of diffusion coefficient on the mobility

$$D = -\frac{\mu c}{q\frac{\partial c}{\partial \phi}} \tag{2.13}$$

where c is the density of states and ϕ is the electrochemical potential. If c obeys to a Maxwell-Boltzmann distribution, i.e. $c \sim exp[-\phi(x)/k_BT]$, the Einstein relation become

$$\frac{D}{\mu} \approx \frac{k_BT}{q} = U_T \tag{2.14}$$

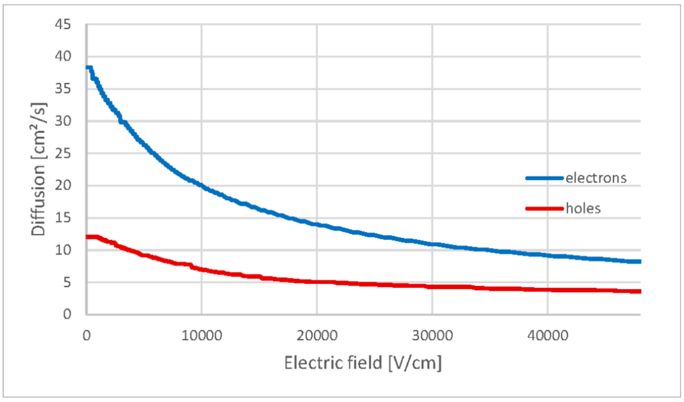

FIGURE 2.9: Electrons and holes diffusion coefficient in silicon detectors (T=300 K). The diffusion coefficient depends on the electric field since it is related to the mobility factor thought the Einstein relation.

where k_B is the Boltzmann constant, T is the operating temperature, and U_T is the thermal potential. With high charge density or low temperature, this approximation is no longer valid [4]. In particular, the treatment of particle concentration pulses leads to Fermi-Dirac distributions. Electrons motion is correlated, and undulatory effects occur between the carriers. Usually a correction factor is calculated or estimated from the experimental data for the interest range.

In a silicon detectors, diffusion motion is relevant to explain the expansion of the initial charge distribution due to particle interaction [5]. The transverse cloud profile is usually described as a 3-dimensional density function that evolves in time [5]

$$\frac{dQ}{dx}(\vec{x},t) = \frac{1}{8(\pi D t)^{3/2}} \int Q_0(\vec{x}')e^{-\frac{(\vec{x}-\vec{x}')^2}{4Dt}}\, d\vec{x}' \tag{2.15}$$

given the initial charge distribution $Q_0(\vec{x})$, and the time t since the interaction happened. If the particle enters orthogonally, the carriers spread out as a Gaussian distribution approximation along the plane of the electrodes (Fig. 2.10). The RMS width σ_D is

$$\sigma_D = \sqrt{2Dt} \tag{2.16}$$

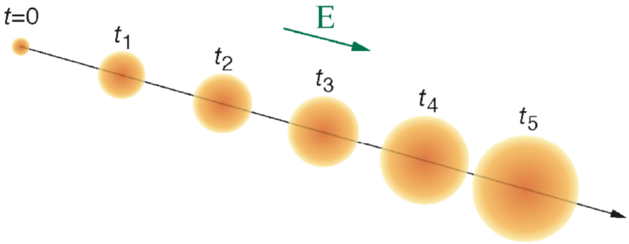

FIGURE 2.10: The charge cloud expands over time due to the diffusion of the carriers in the Silicon. The RMS width depends on the physical properties of the detector. Before all the charges is collected, it generally reaches 10-100 µm. Image from [1].

2.2.2 Commercial implementation: TCAD

TCAD simulators [6] find the solution of transport equations for a semiconductor device model using numerical (Finite Difference / Finite Element) methods. The actual device is represented by a finite number of points in space (mesh), where the characterizing physical quantities are discretized. The equations are solved by evaluating the state at finite-time steps using the boundary conditions of the device. These tools are designed for Microelectronics purposes, and some of them can simulate Single-Event Effects (SEE) or Single-Event Upsets (SEU). A Single-Event consists of a charge particle that interacts with an electronic circuit, and generates enough ionization charges to perturb the logical state of the device.
SYNOPSYS Sentaurus TCAD [7][8] suite contains *HeavyIons* (see Fig. 2.11), a native model to evaluate the SEE at a Device level. The user can define the initial energy profile and the detector structure. The Transient Evolution of the Carriers is simulated, and the output current transient is calculated. In general, results should be considered qualitative, but improving the model precision increases the solution accuracy [9]. The main different between Single-Event and nuclear physics applications lays on the particle energy range and, thus, the number of ionization pairs. In particle detectors, the average linear ionization density and the ionization-pairs density (e.g. ^{12}C 40 MeV generates 8.9×10^5 eV/µm and 10^{16} pairs/cm^3) are considerably larger than for Minimum Ionizing Particle (MIP), typically considered in SEE simulation (e.g. in Silicon 2.6×10^2 eV/µm and 10^6 pairs/cm^3).

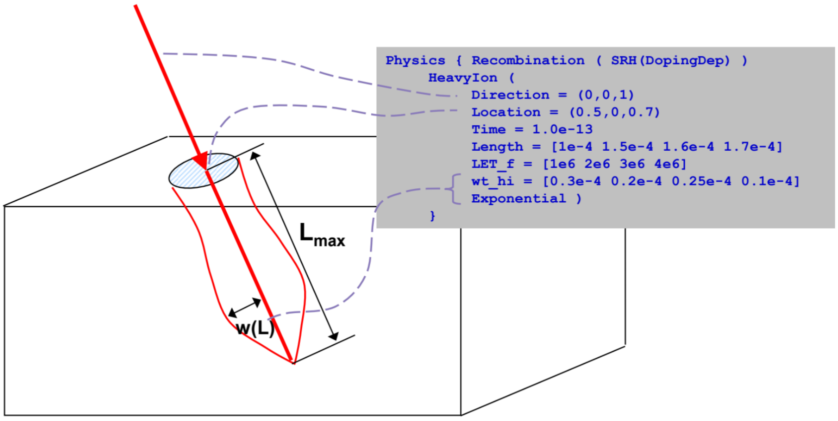

```
Physics { Recombination ( SRH(DopingDep) )
     HeavyIon (
          Direction = (0,0,1)
          Location = (0.5,0,0.7)
          Time = 1.0e-13
          Length = [1e-4 1.5e-4 1.6e-4 1.7e-4]
          LET_f = [1e6 2e6 3e6 4e6]
          wt_hi = [0.3e-4 0.2e-4 0.25e-4 0.1e-4]
          Exponential )
     }
```

Figure 2.11: SYNOPSYS Sentaurus TCAD *HeavyIon* function [8]. This function represents the initial conditions to simulate an high-energy particle interaction. Direction, Location (cm), and Time (ps) define the collision point, angle, and time. Length (cm) is the penetration depth, Wt_hi (cm) represents the distribution width, and LET_f is the linear energy transfer in pair/cm^3. In the example, LET_f and Wt_hi are defined as function of Length: the linear interpolation of the specified values determines the spatial distribution. Exponential or Gaussian chooses the orthogonal pair distribution. Image from [10].

2.3 MicroSil Model

The MicroSil Model is a quasi-microscopic model developed from the Bardelli simulation (2004) [11][12]. The original work is no longer available, but some intermediate code has been used to reproduce and improve their original outcomes. The key idea is to describe the charge transport through the microscopic electrostatic interaction between the carriers. Since the number of electron-hole pairs is incredibly high (see Paragraph 2.2.2), the cluster

approximation is introduced. The original target of this approach is to recreate the "plasma erosion" phenomenon: when the initial electron-hole interaction is strong enough to screen the macroscopic electric field, the charges are difficult to separate, and that affects the carrier collection.
My contribution is centered on model formalization and simulation algorithm development, including a more structured algorithm flow, function improvements, and graphical tools to efficiently elaborate the simulation results.

2.3.1 Initial charge distribution

The model input is the charge density distribution generated by the interaction of a charged particle. The total kinetic energy and the radiation properties define specific ionization profiles in agreement with the Bragg curve. The silicon stopping power, calculated by the Hubert and Schwalm formulae (see [13] and [14]), is used to create a transversal Gaussian distribution of electron-hole pairs with the correct density along the penetration direction. Figure 2.12 displays an example of energy loss with ^{12}C interacting particle.

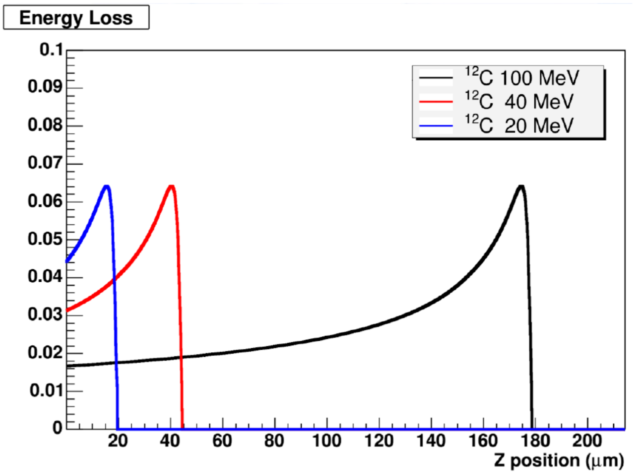

FIGURE 2.12: Calculated Bragg profile of ^{12}C particle. The initial ion energy determines the penetration depth, and the electron-hole pair distribution. Image from [11].

The charge carriers are divided into clusters: a cluster is a uniform spherical charge distribution, defined by position $\vec{p}$, radius R, and total charge Q. The cluster density is the number of clusters in a volumetric unit and obeys the ionization density distribution. The cluster total number is N, and they are equally distributed between negative and positive charge carriers. Each cluster is an independent entity that evolves over time in the detector. The $N/2$ electron clusters have the same charge, determined by the incident particle energy

$$\sum_{i=1}^{N/2}|Q_i|=\frac{N}{2}|Q_1|=\frac{E_n}{\varepsilon} \tag{2.17}$$

where Q_i is the cluster i charge, E_n is the particle ionization energy and ε is the electron-hole pair creation energy (in Si ε=3.6 eV/pair). The holes clusters are created in the same position as the electrons ones, and they have opposite charges. The cluster radii represent the extension of the electrons/holes distribution and they are initially consistent with no positive or negative cluster overlapping principle.

2.3.2 Clusters position evolution (charge drift)

One fundamental hypothesis is that the detector is overdepleted. This assumption leads to consider the free charge density zero along all the detector volume. The second hypothesis is no moving carriers are present in the silicon at equilibrium. The first approximation is accurate when the bias electric field is present along all the device length (overdepletion) since the actual free electrons and holes concentration is near the minority carrier density. The second one is a useful simplification, even if a time-variant leakage current is present in overdepleted detectors.

Under these conditions, the concentration gradient is negligible, and the movement of a charge is due only to the electric field. In every instant, his velocity can be evaluated from the tabulated values of drift velocity in silicon (see Fig. 2.7). The applied electric field $\vec{E}_{ext}$ in the point $\vec{p}$ can be calculated from the operating voltage and the detector properties. In a planar detector oriented along $\vec{z}$ axis

$$\vec{E}_{ext}(\vec{p}) = \frac{2V_{appl}(\vec{p}\cdot\vec{z})}{(\Delta z)^2} + \frac{V_{appl} - V_{depl}}{\Delta z} \tag{2.18}$$

where V_{appl} is the applied voltage, V_{depl} is the depletion voltage, and Δz is the detector thickness. Therefore,

$$V_{depl} = \frac{-q}{2\varepsilon_s}\frac{N_A^- N_D^+}{N_T}(\Delta z)^2 \tag{2.19}$$

where q is the electron charge, ε_s is the silicon permittivity, and N_A^-, N_D^+, and N_T are the doping concentration.

Representing the ionization charge in clusters, the model assumes that the external macroscopic electric field $\vec{E}_{ext}$ and the microscopic electric field $\vec{E}_{mic}$, due to the electrostatic interactions between clusters, generate the total electric field acting on a carrier k.

$$\vec{E}_{tot}(k, \vec{p_k}) = \vec{E}_{ext}(\vec{p_k}) + \vec{E}_{mic}(k, \vec{p_k}) \tag{2.20}$$

where $\vec{p}$ is the position of a cluster. The Coulomb Law describes the interaction between clusters as

$$\vec{E}_{mic}(k, \vec{p_k}) = \frac{1}{4\pi\varepsilon_s}\sum_{h=1}^{N} Q_h \frac{\overrightarrow{\Delta p_{kh}}}{\left|\overrightarrow{\Delta p_{kh}}\right|^3} f\left(\left|\overrightarrow{\Delta p_{kh}}\right|, R_h, R_k\right) \qquad \text{with} \quad \overrightarrow{\Delta p_{kh}} = \vec{p_k} - \vec{p_h} \tag{2.21}$$

where $\vec{p}$ is cluster position, R is the cluster radius, Q is the cluster charge, and $\overrightarrow{\Delta p_{kh}}$ is the distance vector between cluster centers. The correction factor $f(d, R_1, R_2)$ considers the finite dimension of clusters and their overlapping (i.e. if $d \gg R_1 + R_2$, $f \approx 1$, while if $d \ll R_1 + R_2$, $f \approx d$). Even if I have not been able to derive it, the ad-hoc function developed by Bardelli is display.

$$\begin{aligned} f(d, R_1, R_2) = {} & \frac{R_1^6 + R_2^6 + d^6 - 9R_1^4R_2 - 9R_1^4d - 9R_2^4R_1 - 9R_2^4d - 9d^4R_1 - 9d^4R_2}{R_1^3R_2^3} \\ & + \frac{16R_1^3R_2^3 + 16R_1^3d^3 + 16R_2^3d^3 + 18R_1^2R_2^2d^2}{R_1^3R_2^3} \end{aligned} \tag{2.22}$$

The result of this correction should be similar to Fig. 2.13. Other effects are discussed in Paragraph 2.3.5.

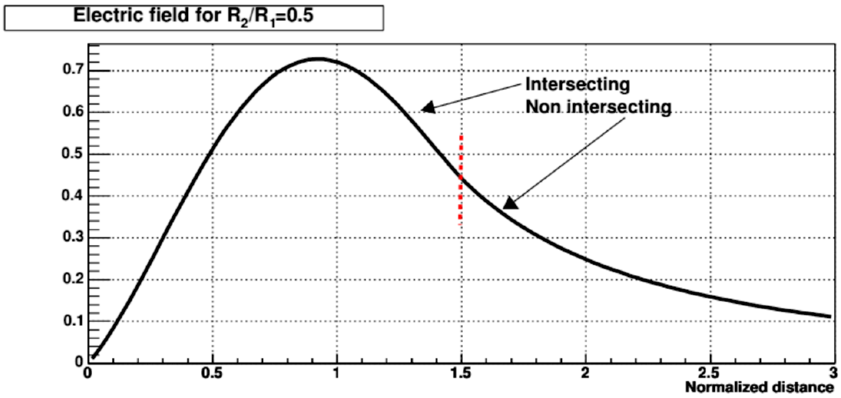

FIGURE 2.13: Example of the correction factor effect with $R_1/R_2 = 0.5$. When the two spherical clusters does not intersect one another, $f \approx 1/d^2$ as expected. In case of intersection, the ratio between the two radii determines how the formula changes. Image from [11].

2.3.3 Clusters collection

The model assumes the clusters drift toward the bias electrodes: the holes towards the p^+ region, and the electrons to the n^+ region. When a cluster reaches the electrodes, its charge is collected. Since the charge carriers density is uniform, the collection process considers the volume fraction outside the detector volume to determine the amount of charge that needs to be removed. The new cluster charge is

$$Q_{t+1} = Q_t(1 - frac) = Q_t \left(1 - \frac{1}{4}\frac{h^2(3R_t - h)}{R_t^3}\right) \tag{2.23}$$

with h the spherical cap height, and $frac$ the volume fraction removed (see Fig. 2.14). The remaining volume is reorganized in a spherical shape with a radius

$$R_{t+1} = \frac{3}{4}\frac{(2R_t - h)^2}{3R_t - h} \tag{2.24}$$

When a cluster is entirely outside the detector, it is considered collected. The cluster position is modified to make the new sphere better approximate the remaining charge density. The model assumes that the electrode collection speed is sufficiently big to not accumulate charge in their proximity.

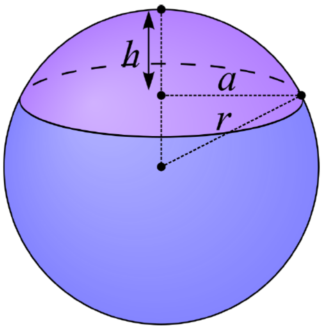

FIGURE 2.14: When a cluster intersects the collection planes, the amount of charge collected (purple) is calculated from the spherical cap volume removed. The remain charge is rearranged in a spherical shape that is tangent to the electrode plain.

2.3.4 Shockley–Ramo Theorem: induced current and charge

The detector readout electrodes generate the output signal. Assuming that only the generated electron-hole pairs are moving, the induced current obeys Shockley–Ramo Theorem [15],

$$I_r = \sum_{i=1}^{N} Q_i \vec{v_i} \cdot \overrightarrow{\mathcal{E}_w}(\vec{p_i}) \tag{2.25}$$

where $\vec{v}$ is the cluster velocity, and $\overrightarrow{\mathcal{E}_w}(\vec{p})$ is the weight field evaluated in the position $\vec{p}$. The weight field differs from the drift field or the applied field. $\overrightarrow{\mathcal{E}_w}$ is obtained by applying a unit potential ϕ_w to the considered electrodes and placing all other ones at the ground. In Figure 2.15 the bias and Ramo potential of a strip detector are displayed. In a plane detector, $\overrightarrow{\mathcal{E}_w}$ is constant and along with $\vec{z}$ axis

$$\overrightarrow{\mathcal{E}_w}(\vec{p}) = \overrightarrow{\mathcal{E}_w} = \frac{\phi_w}{\Delta z} \tag{2.26}$$

From 2.25 and 2.26, in planar detector

$$I_r = \frac{1}{\Delta z} \sum_{i=1}^{N} Q_i \vec{v_i} \cdot \vec{z} \tag{2.27}$$

The induced charge, measured by the electronics, is the integral of the Ramo current

$$Q_r = \int_{t_0}^{+\infty} I_r(t)\, dt = \frac{1}{\Delta z} \sum_{i=1}^{N} \int_{t_0}^{+\infty} Q_i(t) \vec{v_i}(t) \cdot \vec{z}\, dt \tag{2.28}$$

with t_0 the interaction instant. The initial carrier position influences the induced charge measured. Since the ionization distribution depends on the incident radiation, this parameter contains the particle energy information, even if it does not represent an ionization charge measurement.

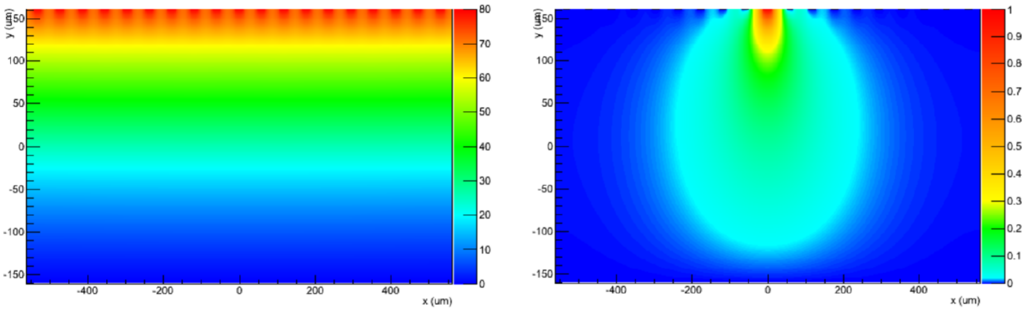

FIGURE 2.15: Representation of the drift (left) and Ramo (right) potential in a strip detector. The weight field differs from the total one since only one electrode is polarized at a time. Image from [16].

2.3.5 Boundary and second-order effects (charge diffusion)

Although the cluster motion is not described using the cluster density gradient, the diffusion affects the cluster expansion. The total ionization charge cloud diffusion obeys (2.15), thus, in the first approximation, the cluster radii similarly enlarge over time. From (2.16) the evolution after δt is

$$R(t+\delta t)^2 = R(t)^2 + kD'\delta t \tag{2.29}$$

D' is the diffusion coefficient evaluated from the local electric field and corrected using some coefficients calculated by Bardelli. For electrons $D' = 1.122235 \cdot D$, and for holes $D' = 1.299472 \cdot D$, with D silicon diffusion coefficient from Fig. 2.9. Since single clusters are considered instead of the total density distribution, the factor $k = 3/5$ is introduced. This behavior is accurate when the clusters are spread out, and, thus, there is a difference between the cluster charge density and the neighboring region one. When the clusters are packed, the diffusion is intuitively limited by the other clusters, and this effect needs to be considered in the model implementation.

The detector structure leads to the presence of two conductive plates on the silicon bulk. This configuration defines the boundary condition for the electric field calculation. When a charge is near a conductive surface, its electric field is different from the free-space one. The effect, according to the Method of Mirror Charges, can be obtained using an infinite number of mirror copies. Each cluster generates an inverted-charge one in every mirror volume. The microscopic field formula (2.21) should consider all the mirrors

$$\vec{E}_{mic}(k,\vec{p_k}) = \frac{1}{4\pi\varepsilon_s}\sum_{i=-\infty}^{+\infty}(-1)^i\sum_{h=1}^{N} Q_h \frac{\overrightarrow{\Delta p_{kh}}+i\overrightarrow{\Delta z}}{\left|\overrightarrow{\Delta p_{kh}}+i\overrightarrow{\Delta z}\right|^3} f\left(\left|\overrightarrow{\Delta p_{kh}}+i\overrightarrow{\Delta z}\right|, R_h, R_k\right) \tag{2.30}$$

where $\overrightarrow{\Delta z}$ is a vector along $\vec{z}$ with norm equal to the detector thickness. Since increasing the distance d makes the Coulomb Force decrease like $1/d^2$, only the first mirror volumes affect the electric field value, and, then, the relevant clusters are those shown in Figure 2.16.

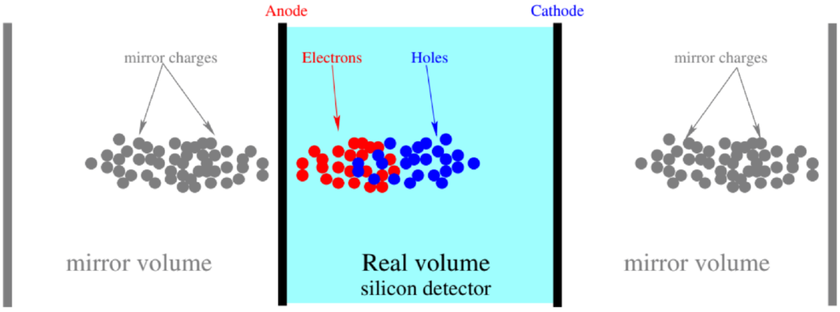

FIGURE 2.16: During the electric field calculation, the boundary conditions are considered using opposite charges mirrored by the electrode plains. Only the first order mirror clusters are necessary to obtain precise enough result. Image from [11].

Even if the detector is overdepleted, the high-doped regions n^+ and p^+ are big carrier tanks, and their concentration remains invariant (Fig. 2.17). Usually, these zones are thin (∼1 µm) compared to the bulk thickness, and they keep exchanging electrons with the electrodes (reversed bias current). A charge that enters these regions is considered collected. In underdepleted detectors, the region near the negative electrode has low electric field, and some holes can remain trapped between the n^+ region and the incoming ionization electrons. These positive charges slowly drift toward the positive electrode, and prevent a fast collection of the electrons. This phenomenon is relevant with low-energy heavy ions since more charges are generated near the electrode.

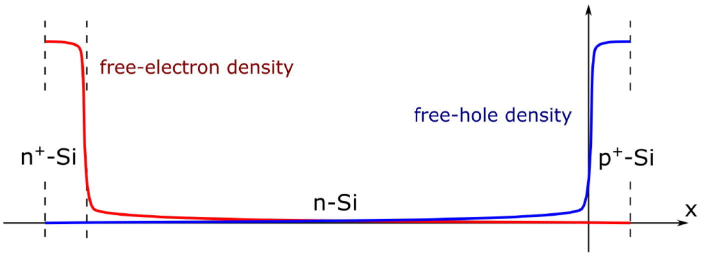

FIGURE 2.17: Free charge density of over-depleted n^+-n-p^+ junction. While the carrier concentration in the active volume is negligible, in the heavily doped region it is not. When the ionization charges reach these regions, they are considered collected.

A different phenomenon occurs when the interacting ion is an high-Z one. The initial high charge density and the electron mobility, higher than the holes one, lead to the "plasma-erosion", illustrated in Fig. 2.18. At the beginning, the Coulomb Force sticks together the high-density parts of the two distribution, and the action of the macroscopic field is shielded. The applied field can only erode the cluster cloud borders until the charge densities are sufficiently reduced.

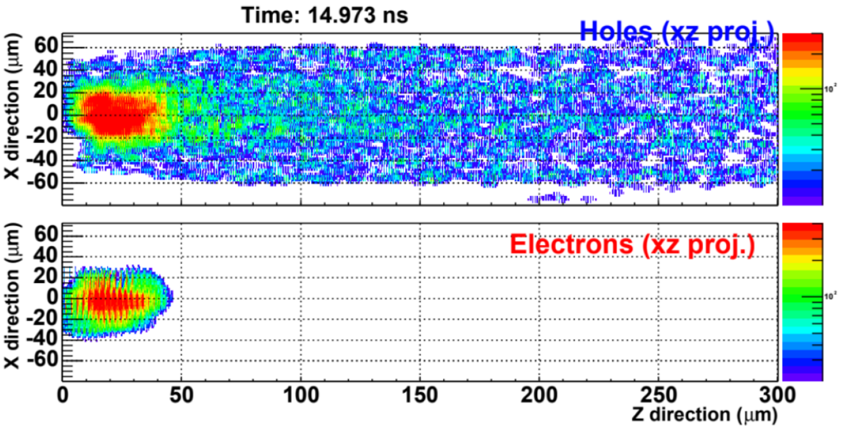

FIGURE 2.18: Simulated plasma erosion with 40 MeV ^{12}C ion. The external electrons have been rapidly collected while the holes are shielding the internal negative charges from the bias electric field. The process ends when enough clusters are collected. Image from [11].

2.3.6 Known limits of validity

The most important limitation is the bias voltage. For detectors polarized with a voltage near or under the depletion one, the free charge concentration is no longer negligible near the negative electrode. In these cases, the charge motion is no correctly simulated, and the charge collection time may result slower than the actual one.

Charges recombination along their path is not considered in the model. All the charge generated in the particle interaction is only removed when it reaches the detector bounds.

Impurity, not uniform doping, which can lead to electric field fluctuations, and channelling effect are disregard. Bias voltage and current are also supposed constant.

Even if the output signals are modelled, the readout chain effects are not taken into account: that depend on the experimental apparatus and are not a priori negligible. Usually the integration time slows down the measured signals and introduces other deformations.

MicroSil simulation 3

3.1 Model implementation

The MicroSil model is implemented in a simulation program. The code is written in C/C++, and some external packages are used. ROOT library [17] is used to perform data analysis and to handle the graphical interface. The simulation inputs are the Physics parameters of the system and the interaction properties. The configuration parameters are estimated by comparing the simulation results with experimental signals. The simulation output consists in Ramo current and charge signals.
The code structure is sketched in Fig. 3.1. In the next paragraphs, the main aspects of the model implementation are presented and discussed.

3.1.1 Physics parameters (detector and particle)

The main configurable inputs related to physical properties are:

DET_THICKNESS Detector bulk thickness in µm.

DET_VAPPL Operating voltage (V).

DET_VDEPL Deplation voltage (V). The estimation of this parameter is presented in Paragraph 4.1.1.

ION_Z Atomic number of the incident radiation.

ION_A Mass number of the incident radiation.

ION_E Particle ionization energy in MeV. The ionization energy per nucleon is obtained by ION_E/ION_A.

TRACK_ANGLE_DEG Incident particle angle from the detector surface normal.

DET_ISREVERSE True when the particle enters the low-field side. The detector configuration is named *reversed*, and it is usually chosen in Pulse Shape Analysis (PSA) to obtain delayed signals.

The charge mobility (Fig. 2.7) and diffusion coefficient (Fig. 2.9) tables can also be redefined.

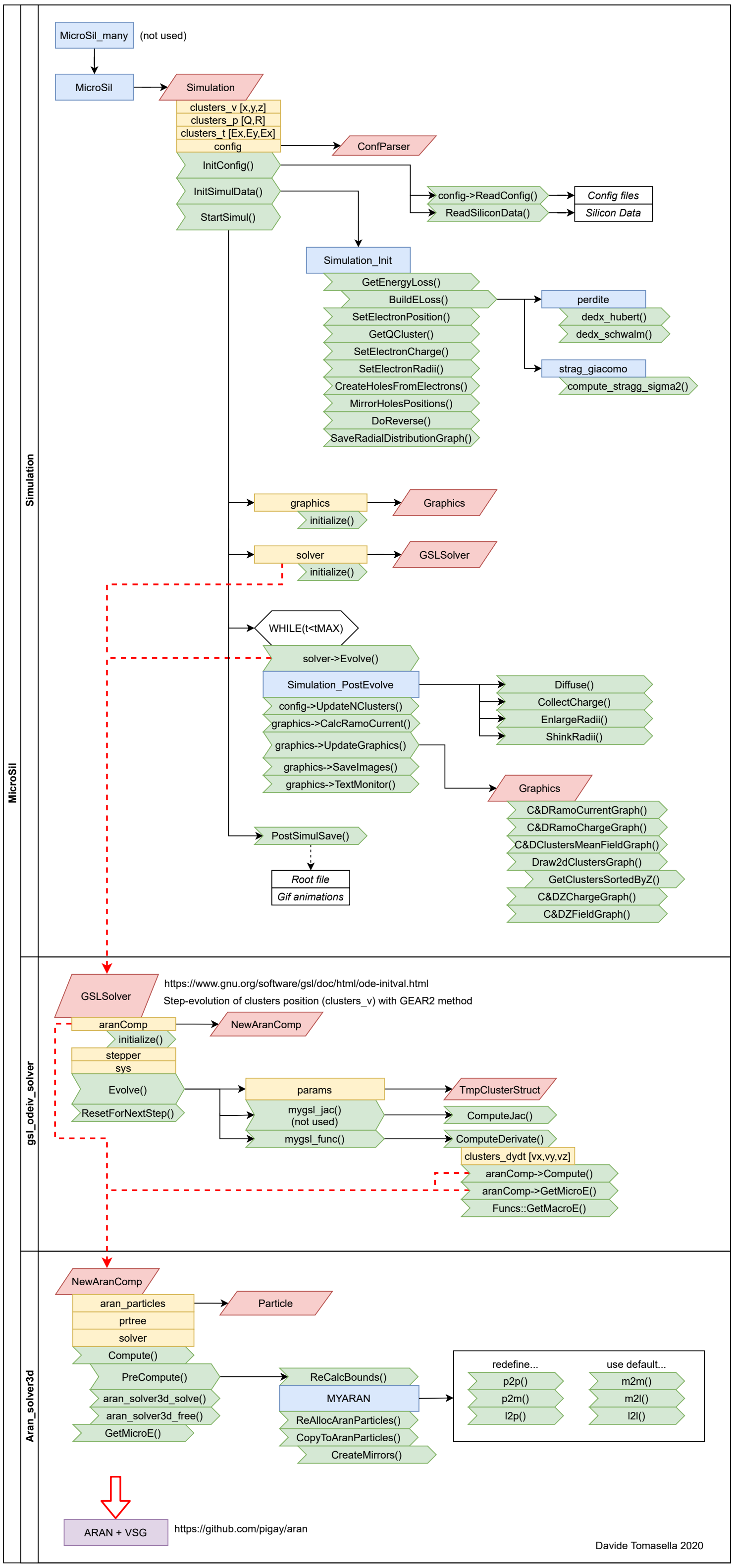
MicroSil
Simulation
MicroSil_many
(not used)
MicroSil
Simulation
clusters_v [x,y,z]
clusters_p [Q,R]
clusters_t [Ex,Ey,Ex]
config
ConfParser
InitConfig()
InitSimulData()
StartSimul()
config->ReadConfig()
ReadSiliconData()
Config files
Silicon Data
Simulation_Init
GetEnergyLoss()
BuildELoss()
SetElectronPosition()
GetQCluster()
SetElectronCharge()
SetElectronRadii()
CreateHolesFromElectrons()
MirrorHolesPositions()
DoReverse()
SaveRadialDistributionGraph()
perdite
dedx_hubert()
dedx_schwalm()
strag_giacomo
compute_stragg_sigma2()
graphics
initialize()
Graphics
solver
initialize()
GSLSolver
WHILE(t<tMAX)
solver->Evolve()
Simulation_PostEvolve
config->UpdateNClusters()
graphics->CalcRamoCurrent()
graphics->UpdateGraphics()
graphics->SaveImages()
graphics->TextMonitor()
Diffuse()
CollectCharge()
EnlargeRadii()
ShinkRadii()
Graphics
C&DRamoCurrentGraph()
C&DRamoChargeGraph()
C&DClustersMeanFieldGraph()
Draw2dClustersGraph()
GetClustersSortedByZ()
C&DZChargeGraph()
C&DZFieldGraph()
PostSimulSave()
Root file
Gif animations
gsl_odeiv_solver
GSLSolver
https://www.gnu.org/software/gsl/doc/html/ode-initval.html
Step-evolution of clusters position (clusters_v) with GEAR2 method
aranComp
initialize()
NewAranComp
stepper
sys
Evolve()
ResetForNextStep()
params
TmpClusterStruct
mygsl_jac()
(not used)
ComputeJac()
mygsl_func()
ComputeDerivate()
clusters_dydt [vx,vy,vz]
aranComp->Compute()
aranComp->GetMicroE()
Funcs::GetMacroE()
Aran_solver3d
NewAranComp
aran_particles
prtree
solver
Compute()
Particle
PreCompute()
aran_solver3d_solve()
aran_solver3d_free()
GetMicroE()
ReCalcBounds()
MYARAN
ReAllocAranParticles()
CopyToAranParticles()
CreateMirrors()
redefine...
p2p()
p2m()
l2p()
use default...
m2m()
m2l()
l2l()
ARAN + VSG
https://github.com/pigay/aran
Davide Tomasella 2020

FIGURE 3.1: Simulation code structure and dependencies. The program simulates the detector signal generation by implementing the MicroSil Model (see Paragraph 2.3). The key external libraries are GSL2 (see Paragraph 3.1.3) and LibAran (see Paragraph 3.1.4).

3.1.2 Simulation initialization

In the initialization phase, the silicon stopping power for the ion, and the energy-loss distribution are calculated. In the configuration file, the cluster number N is selected: NCLUSTERS_PER_MEV determines the carrier number per unit of ionization energy (MeV). Appropriate values lead to $N \sim 10^3$-10^4. The cluster information are stored in an array of structures:

CLUSTERS_V [x, y, z] contains the cluster center position.

CLUSTERS_P [R, Q] contains cluster radius and charge.

CLUSTERS_T [Ex, Ey, Ez] contains the local electric field at cluster position.

3.1.3 ODEIV solver (Gear Method) for model evolution

The time evolution of the clusters is performed using an Ordinary Differential Equation (ODE) [18] solver. The library GSL2 [19] provides the package ODEIV to solve n-dimensional first-order problems

$$\frac{dy_i(t)}{dt} = f_i(t, y_1(t), ...y_n(t)) \qquad with \quad i = 1, ...n \tag{3.1}$$

A numerical solver implements the functions to make the system evolve from its initial state to the next one by a finite time step. Different solving methods can be chosen knowing the system properties, i.e. the real physical system associated with the model.

The Initial Value Problem (IVP) associated with the MicroSil model is a non-linear stiff problem. The variable y is a $3N$-elements vector (N is the cluster number) containing the cluster positions. Its derivate is actually the cluster velocity dy/dt, and the function f calculates the velocity dy/dt by evaluating the electric field at the position y (see (2.7), (2.8) and (2.20)). The non-linearity is due to Coulomb Force in the microscopic field formula (2.21). The stiffness is a system property: the maximum step-size is determined by the largest eigenvalue, while the integration time for full evolution of the solution is governed by the smallest eigenvalue (slowest decay rate). With MicroSil the stiffness property is accounted by considering the small-scale effects of the inter-cluster interactions (fast dynamics, large eigenvalue) added to the macroscopic drift due to the applied electric field (slow dynamics, small eigenvalue).

These are well-known problems in the literature that can be solved through variable-step implicit methods, i.e. the Backward Differentiation Formula (BDF) [18]. The BDF belongs to the linear multistep method family: the information about the solution and its derivative at more than one point is used to extrapolate the next point. It is possible by approximating the function f with a k-grade polynomial, and the approximate solution is shown as

$$\bar{y}^{n+1} = \sum_{i=0}^{p} \bar{a_i} \cdot \bar{y}^{n-i} + h \sum_{i=-1}^{p} \bar{b_i} \cdot \bar{f}(t^{n-1}, \bar{y}^{n-i}) \tag{3.2}$$

where p depends on the order k as $2p + 3 \geq k + 1$. The coefficient $b_{-1} \neq 0$ leads to an implicit formula, necessary to obtain a stable solution in stiff problems.

By varying at each calculation the time-step and the order k, the error is kept below a user-defined threshold. Gear Method [20] M=2 is adopted since the system dimension, specified by the cluster number, is very high (tipically greater than 1-10 $\times$ 10^3), and its GSL implementation does not require the computation of the Jacobian $N \times N$ matrix of the function f. Furthermore, while the cluster collection proceeds, the system dimension changes making expensive the Jacobian usage.

3.1.4 FMM (Fast Multipole Method) for cluster interactions

While the macroscopic field formula (2.18) has time complexity $O(1)$, the calculus of the microscopic electric field, performed using (2.21) (2.30) formulae, requires $O(N^2)$ operations. The computation of the forces between several particles is known as the N-body problem, and can be solved efficiently ($O(N)$) using the Fast Multipole Method (FMM) [21][22]. The simulation algorithm uses LibAran [23][24].
The method uses tree structures (OcTree [25] in LibAran) to break the problem into smaller subproblems following the divide-and-conquer paradigm. Each level of the tree approximates the child node and leave information (i.e. charge and position) to reduce the computational time of the problem. In the FMM algorithm, this process is more complicated because the relative position between the node centers influences the interaction type. The FMM assumes the potential ϕ of the considered field can be express as

$$\Phi = \Phi_{ext} + \Phi_{near} + \Phi_{far} \tag{3.3}$$

where Φ_{near} is a rapidly decaying function of distance, Φ_{far} is the far-field potential (Coulombic or gravitational), and Φ_{ext} is independent of the particle number. Excluding the external contribution, all the potential can be reformulated using the spherical harmonics as

$$\Phi = \sum_{n=0}^{\infty} \sum_{m=-n}^{n} \left(L_n^m r^n + \frac{M_n^m}{r^{n+1}} \right) Y_n^m(\theta, \phi) \tag{3.4}$$

where r, θ, and ϕ are the spherical coordinates, the terms $r^n Y_n^m(\theta, \phi)$ are spherical harmonics of degree n, the terms $Y_n^m(\theta, \phi)/r^{n+1}$ are spherical harmonics of degree $-n-1$, and the coefficients L_n^m and M_n^m are the moments of expansions. The far-field (multipole) expansion is given by the M_n^m terms while the local expansion by L_n^m ones. The spherical harmonics are then expressed through the Legendre functions

$$Y_n^m(\theta, \phi) = \sqrt{\frac{2n+1}{4\pi} \frac{(n-|m|)!}{(n+|m|)!}} \cdot P_n^{|m|}(\cos\theta) e^{im\phi} \tag{3.5}$$

Given the multipole and the local expansions, some transformation matrices calculate a node effect on another, transferring the information through the tree (see Fig. 3.2). The approximation is chosen by limiting the harmonic series and the OcTree levels number.

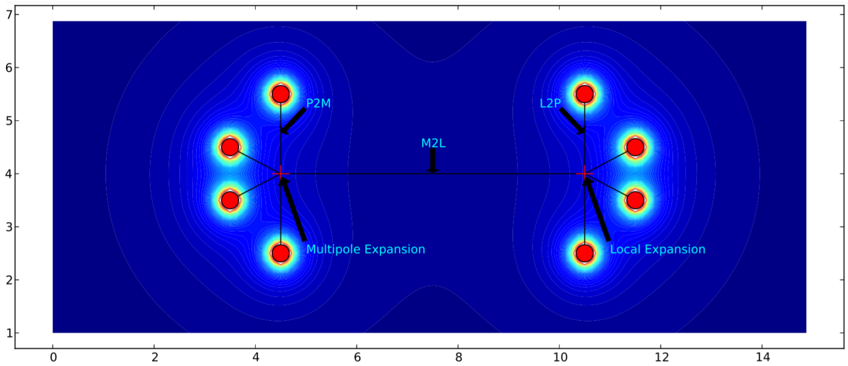

Figure 3.2: Graphical representation of the Fast Multipole Method. The Multipole and Local Expansion represent the contribution of far and near charges to the total field on a given node. The transformation matrices P2M (pole to multipole), M2L (multipole to local), and L2P (local to pole) transfer the contribution of the other nodes to the considered one. Image from [26].

The MicroSil model operates with clusters, and the MICRO_FACTOR parameter scales the result of the FMM calculation. The spherical charge distribution effects on the local field have to be considered in the function that describes the particle-to-particle interaction. The simpler approximation is: if one cluster is inside another (more precisely if $d \leq (R_1 + R_2)/2$) the Coulomb Force is negligible. The formulation which I have implemented approximates (2.22) as following:

$$\frac{\vec{d}}{d^3} f(d, R_1, R_2) = \begin{cases} \frac{\vec{d}}{d^3} & \text{if } d > k(R_1 + R_2) \\ \frac{\vec{d}}{[k(R_1+R_2)]^3} & \text{if } d \leq k(R_1 + R_2) \end{cases} \tag{3.6}$$

where $k = (1 + R_{min}/R_{max})/2$. Other effects due to the finite cluster radii are described in the next section.

3.1.5 Post-evolve operations

For each time-step of the ODE solver, the cluster positions (and the electric field) are updated several times. The max time-step is fixed at 1 ns to perform other operations with no loss of precision. After each step, the cluster radii are increased as described in (2.29). Moreover, two functions are implemented to correct the non-physical overlapping of the same carrier type (electrons or holes) in the initial time, without modifying the global diffusion rate. These functions enlarge and shrink the radii keeping unvaried the proportion between them. This process also creates the Gaussian distribution of charges as the clusters near the center of the plasma column expand slower than the external ones.

The other functions control the charge collection as described in Paragraph 2.3.3. When the cluster is collected, the corresponding data structure is deleted. On the other hand, when a cluster moves against the macroscopic electric field force and reaches the high-doped zones (see Paragraph 2.3.5), it is reintroduced in the detector volume. The new position is randomized and depends on the electric field near the electrode, behaving differently with underdepleted detectors, and the parameter REDUCE_SQUASH defines the relative amount of charge that is contained in the new cluster.

3.1.6 ROOT for graphical interface

The simulation terminates when all the charges have been collected or when a max time has elapsed. The main output of the simulation is the electric signal induced at the readout electrodes. It is calculated using the Ramo Theorem (2.27) (2.28) from the cluster velocity and then saved in a ROOT file. To monitor the simulation is also used the ROOT package to display the most meaningful graphs, as displayed in Fig. 3.3. The interface shows the current and charge signals induced by the electrons (red) and holes (blue) motion, the components (red, green and blue) and the module (black) of the mean electric field at the cluster positions, the z-component of the electric field generated by the carriers (black) and the bias voltage (red) along with the $\vec{z}$ axis, and the 1-dimensional and 2-dimensional cluster distribution (negative charges in red and positive ones in blue).

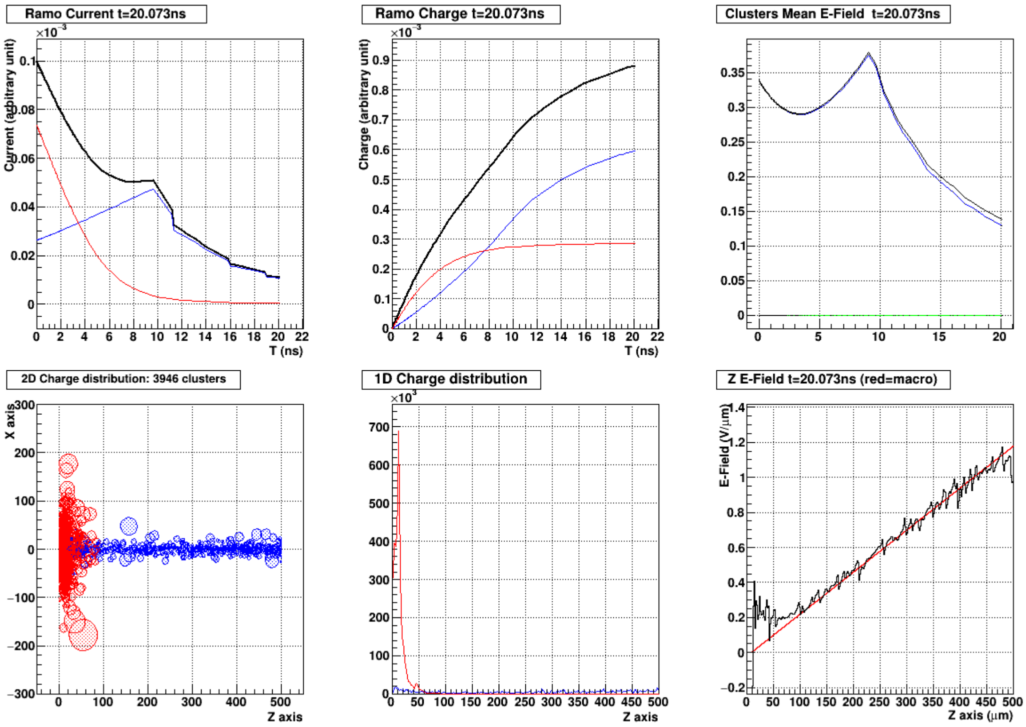

Figure 3.3: Graphical interface of the MicroSil simulation. The different graphs, updated over time, show evolution of the simulation. The final results are than saved in a ROOT file. See Paragraph 3.1.6 for details.

3.2 Simulation setup

Scripts have been developed to run a large number of simulations. Some of them compare the experimental data with the simulated one, and consider the acquisition chain effects on the signals. Automatizing these operations aids to the estimation of the model parameters: the MicroSil model contains some variable parameters since some physic effects are not considered in the cluster approximation. Defining which parameters are not fixed by the Physics formulae is fundamental to make the simulation match the expected result.

3.2.1 Configuration files generation and parameterization

The simulation configuration file generation is automatized thanks to some parametric scripts. Launching multiple simulations is essential to observe, in a limited time, how the model parameters influence the simulation. The parameters that have a large impact on the results are the MICRO_FACTOR and the REDUCE_SQUASH while increasing the DIFFUSION_FACTOR does not have relevant effects. Choosing an appropriate NCLUSTERS_PER_MEV is necessary to obtain precise enough output signals. Nevertheless choosing NCLUSTERS_PER_MEV too large introduces undesidered effects (see Paragraph 4.2.2).

Other relevant parameters are the DET_VAPPL and DET_VDEPL since they define the macroscopic field inside the detector (2.18). The DET_VDEPL needs to be estimated through experimental measurements (see Paragraph 4.1.1).

Selecting the same parameters, the variability in the simulation results is limited to the charge distribution graphs, and the output signal fluctuations are negligible.

3.2.2 Output generation and acquisition chain effects

Other scripts manage the output files when multiple simulations have been run: it is necessary when different parameter configurations need to be tested together. The comparison with the experimental signals and the parameters optimization are performed thanks to them.
With the comparison between the simulated signals and the experimental ones, some systematic errors are introduced by the acquisition chain. In particular, preamplifier response, cable integration, and digitizer anti-aliasing filter are the dominant noise sources. The step response of the acquisition chain $y_{step}(t)$ is measured to consider all these effects, and the convolution between the step response and the induced current leads to a charge signal comparable with the experimental ones. From the convolution properties

$$\begin{aligned} Q_{chain}(t) &= Q_{sim} * y_{imp}(t) = Q_{sim}(t) * \frac{dy_{step}(t)}{dt} = \frac{dQ_{sim}(t)}{dt} * y_{step}(t) = \\ &= I_{sim}(t) * y_{step}(t) \end{aligned} \tag{3.7}$$

3.2.3 Signal likelihood indices

To evaluated the quality of the simulation and the correctness of the MicroSil model, two matching indices are determined. Since the incident particle energy, a simulation input parameter, is obtained from the maximum value of the charge signals, the comparison between simulated and experimental signals is performed using normalized signals.
The first index is the MSE (Mean Square Error) between the signals. This index is calculated over 300 samples of the two signals since the experimental waveform sample time is 10 ns (see Paragraph 4.1.1 and 4.1.2), and it represents a good estimation of the likelihood. The alignment between the two signals is performed minimizing the MSE.

$$MSE_{al} = \sum_{k=1}^{300} \left(Q_{chain}(kT_s - T_1) - Q_{exp}(kT_s - T_2)\right)^2 \tag{3.8}$$

where Q_{chain} is the simulated signal with the acquisition chain effects, Q_{exp} is the experimental one, T_s is the sampling step, and T_1, and T_2 are the offset times. The same information can be displayed by the MSE_{dB}

$$MSE_{dB} = 10 \log_{10}(MSE_{al}) \tag{3.9}$$

and the $RMSE$ (Root Mean Square Error)

$$RMSE = \sqrt{(MSE_{al})} \tag{3.10}$$

The second index is the rise time difference (Δt_r) between the two signals. The rise time is considered because it is an important parameter to discriminate the incident radiation in the PSA (Pulse Shape Analysis).

$$\Delta t_r = |t_r(Q_{chain}) - t_r(Q_{exp})| \tag{3.11}$$

Simulation results and comparison with experimental data 4

4.1 Experimental setup and collected data

The experimental signals, that are evaluated in the simulation analysis, are collected with EUCLIDES [27] and FAZIA [28] setups. At LNL, I tested EUCLIDES telescopes, consisting of 147-µm and 1000-µm silicon detectors, by collecting waveforms from ^{241}Am α source. The FAZIA dataset contains signals waveforms of charged particles up to Z=22, stopped in a 500-µm Si detector. The different setups and particles have provided a large number of configurations that have been tested with the simulation results.

4.1.1 EUCLIDES detectors

The EUCLIDES array is made up of two-stage ΔE-E telescopes, arranged in a 42-face polyhedron. Each telescope consists in a 147-µm ΔE detector and a 1000-µm E detector, separated by a 100-µm Kapton spacer. The preamplifier boards (scheme in Fig. 4.1) are placed outside the vacuum chamber, and they also provide a filtered bias voltage to the detectors. The charge-sensitive preamplifier input is a low noise junction field-effect transistor (JFET) (see Paragraph 2.1.3). The output is provided by a differential amplifier. The output dynamics is ± 4.5 V with a sensitivity of 45 mV/MeV (the energy range is up to 100 MeV). The signal are acquired by 14-bits ADC boards with a sampling rate of 100 MHz. A number of 20k traces is considered to obtain the experimental signals for the simulation comparison.

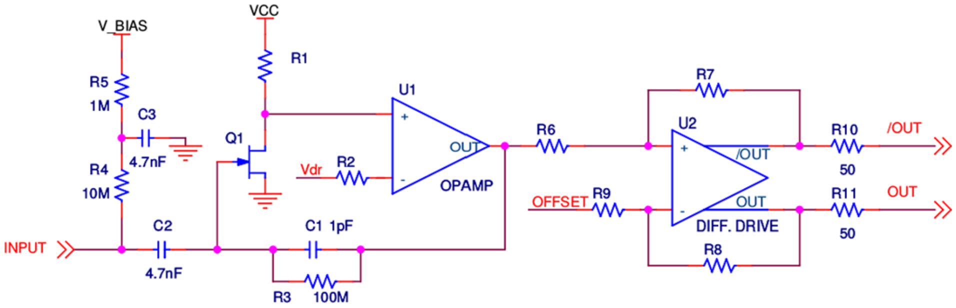

FIGURE 4.1: Scheme of the EUCLIDES charge-sensitive preamplifier. Image from [27]

I used a test setup with new silicon detectors and the EUCLIDES preamplifier boards. The detectors are placed in a vacuum chamber in reversed configuration near an ^{241}Am source emitting 5.485 MeV α particles. The preamplifier is connected to the digitizer through shielded cables.
An external pulse, with a ∼9 ns rise time, is injected at the preamplifier to characterize the electronics read-out chain. The response is also affected by the cable integration and some reflections between digitizer and preamplifier board, as shown in Fig. 4.2. The test setup with the 147-µm detector also introduces some oscillations in the output signals because the detector equivalent capacitance is not taken into account during this acquisition. With the E detector, the ∼1000-pF capacitance does not affect the system pole position, while the capacitance of the ΔE detector (∼100 pF) creates a complex pole in the system, and reduces the range where the charge preamplifier operates as an integrator.

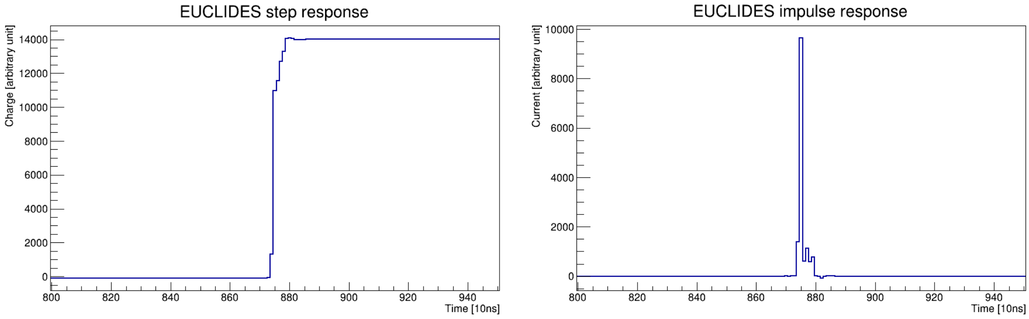

FIGURE 4.2: Step and impulse response of EUCLIDES test acquisition chain.

The two detectors are operated with different operating voltage, while the depletion one is measured by evaluating the I-V characteristic of the inverse bias junction. The characteristics are reported in Fig. 4.3. The 147-µm detector is fully depleted applying ∼12 V, while the *plateau* in the 1000-µm one is not well-defined, and the depletion voltage is difficult to estimate. Different values are considered in the simulation analysis between 130 V and 180 V.

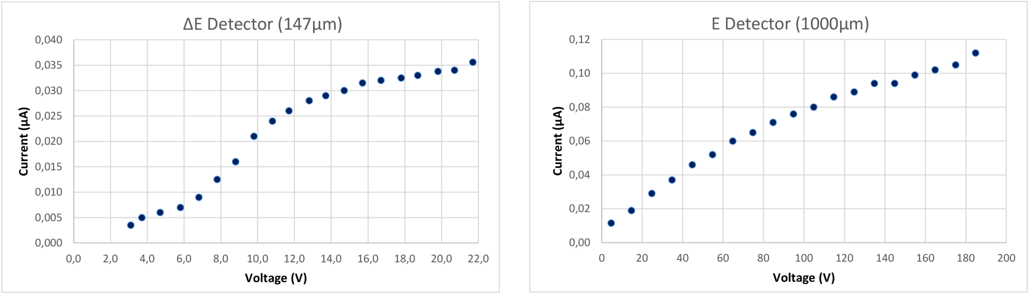

FIGURE 4.3: I-V characteristic of ΔE (left) and E (right) EUCLIDES detectors. The depletion voltage is defined as a slope change in the characteristics.

4.1.2 FAZIA dataset

The FAZIA apparatus consists of several telescopes, aiming at a 4π coverage. Each telescope is made up of a 300-µm ΔE detector and a 500-µm E detector, and a CsI(Tl) crystal photodiode. Different energy-range particles stop in the different telescope parts, and the particle loci can be obtained with different methods, e.g. ΔE-E correlation, E-I_{max}, E-t_r.

The FFE (Front-End Electronics), displayed in Fig. 4.4, is directly connected to the telescope, and the traces are digitized in place. The available dataset contains particles that have stopped in the E detector. These signals are sampled at 100 MHz with a 14-bits ADC, the output dynamics is 4 GeV. Since the initial energy loss only reduces the particle velocity (see Paragraph 2.1.2), the interaction with the ΔE detector can be neglected by considering particles with lower energy entering only the E detector.

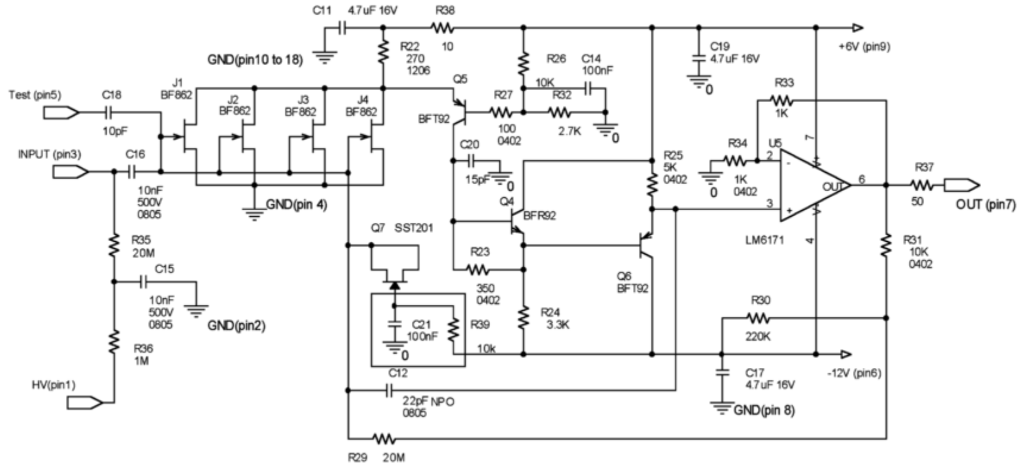
C11 4.7uF 16V
R38
R22 270 1206
10
GND(pin10 to 18)
R26 10K
C14 100nF
R32 2.7K
C19 4.7uF 16V
+6V (pin9)
Test (pin5)
C18 10pF
J1 BF862
J2 BF862
J3 BF862
J4 BF862
Q5 BFT92
R27 100 0402
R33 1K
C20 15pF
INPUT (pin3)
C16 10nF 500V 0805
GND(pin 4)
R25 5K 0402
R34 1K 0402
U5
OUT
R37 50
OUT (pin7)
Q4 BFR92
Q7 SST201
LM6171
R35 20M
C15 10nF 500V 0805
GND(pin2)
R23 350 0402
R24 3.3K
Q6 BFT92
R31 10K 0402
C21 100nF
R39 10k
R30 220K
R36 1M
C12 22pF NPO 0805
C17 4.7uF 16V
-12V (pin6)
GND(pin 8)
HV(pin1)
R29 20M

Figure 4.4: Scheme of the FAZIA FFE. Image from [29]

The step response (Fig. 4.5) is acquired using the internal pulse generator with a 10-cm Kapton and a 100-pC capacitor to simulate the detector. The response does not show peculiar disturbs, and, thus, the acquisition chain noise is very low, compared to the EUCLIDES one. The applied voltage (~290 V) is near the depletion one, but the precise I-V characteristic has not been acquired.

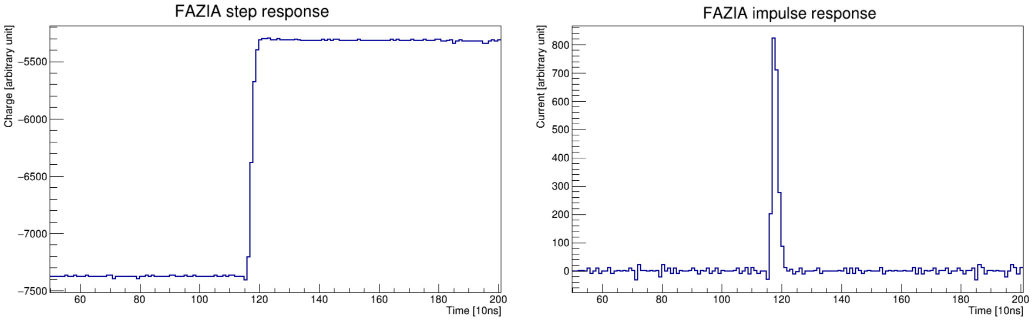

Figure 4.5: Step and impulse response of EUCLIDES test acquisition chain.

The dataset consists of charged ions with energy up to ~30 MeV/u, generated from a ^{20}Ca beam. The traces are already classified by considering the loci in the ΔE-E correlation graph. The experimental waveforms, over a small range of energies centered on the simulated particle energy, are meant to obtain the experimental signals.

4.2 Analysis of simulated and experimental signals

The analysis involves α particles (5.485 MeV and 21.940 MeV) and light ions (Z up to 13) of variable energy. The experimental dataset considers the EUCLIDES 147-µm and 1000-µm detectors (see Paragraph 4.1.1) with different bias voltage and the FAZIA 500-µm detector (see Paragraph 4.1.2). The different detector properties, average ionization density (e.g: 2.2×10^5 eV/µm and 1.23×10^6 eV/µm with the α), and number of generated electron-hole pair (e.g. 1.5×10^6 pairs and 6.1×10^6 pairs with the considered α), give a large application range to study the effects of the main parameters on the simulated signals. The tested configurations include only particles that enter the silicon in the low electric-field region, i.e. detectors in reversed configuration, since this is the typical approach in PSA applications. The comparison with the experimental traces is performed using the indices presented in Paragraph 3.2.3, and the simulation results are then evaluated.

4.2.1 Description of the signal formation

The description of the cluster motion, thanks to the simulation graphical interface (see Fig. 4.6 and Fig. 4.7), is fundamental to understand how the characteristics of the current and charge signals are influenced. Furthermore, this analysis leads to a better comprehension of the phenomena that occur with different ions and higher energies.
Even if the collection time may differ due to many factors, the following general discussion considers all the "collection phases" that the studied configurations have in common:

PEAK SEPARATION The electron and hole distributions start separating each other and moves toward the respectively collecting electrodes. In this phase, the interaction between the charge carriers is still predominant, and the charge cloud needs to expand more before the bias electric field prevails.

FAST ELECTRON COLLECTION In the reversed configuration, the ion enters the electrode in the lower potential zone. In the first nanoseconds, the electrons near the entering electrode are quickly collected, while the *plasma column* starts diffusing. The fraction of electrons immediately removed depends on the penetration depth since only those next to the electrode are taken off before the holes expand.

HOLE MOTION Due to the different mobility factors of electrons and holes, the holes are still in the high-field region when the electrons reach the entering electrode. There, the negative charges slow down because of the low electric field value and the holes that have not started moving yet. If the electron density is high enough, it interacts with the holes still in the low-field region and it also slows down their collection process.

HOLE PEAK COLLECTION The holes are moving to the region with the higher electric field, and the induced current increases. The charges drift with different velocities because of the non-uniform bias electric field and the Coulomb Forces. When the holes Bragg peak is collected, the main fraction of the total charge is absorbed.

HOLE TAIL COLLECTION The remaining positive charges are slowly attracted to the collecting electrode. This process is relevant when the initial charge distribution length is comparable with the detector thickness, e.g. with higher energy particles, since more charges are generated outside the Bragg peak, and the peak is collected faster.

SLOW ELECTRON COLLECTION When the hole density in the low-field region is low enough, the electrons restart moving toward the electrode. In devices with operating voltage below or near the depletion one, this motion can be very slow because the macroscopic field action is limited and the charges have already diffuse enough to minimize the repulsive forces between them.

END OF COLLECTION The collection process ends when all the remaining electrons are taken out of the detector. Even if the particle interaction generates the same number of electrons and holes, their contribution to the output signals can be very different. In particular, if the particle has low energy and stops near the entering electrode, the holes generate the most of the induced charge since they have to move through the whole detector.

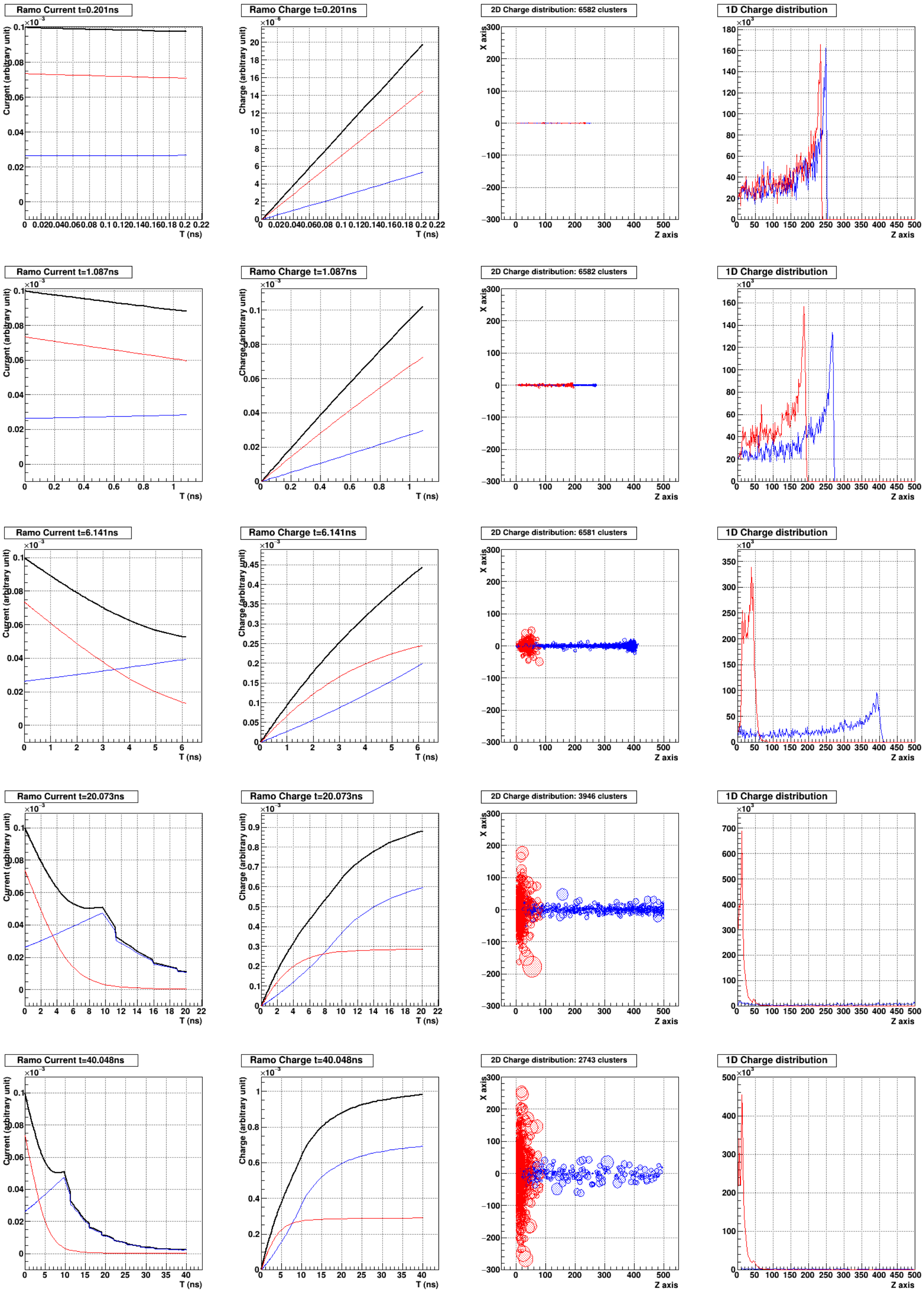

FIGURE 4.6: Collection process with 500-µm detector and 21.940 MeV α. The current and charge signals and the charge distribution are shown at several time instant (0.2 ns, 1 ns, 6 ns, 20 ns, and 40 ns) after the particle interaction. The electron and hole motion generates the output signals of the detector. See Paragraph 4.2.1 for details.

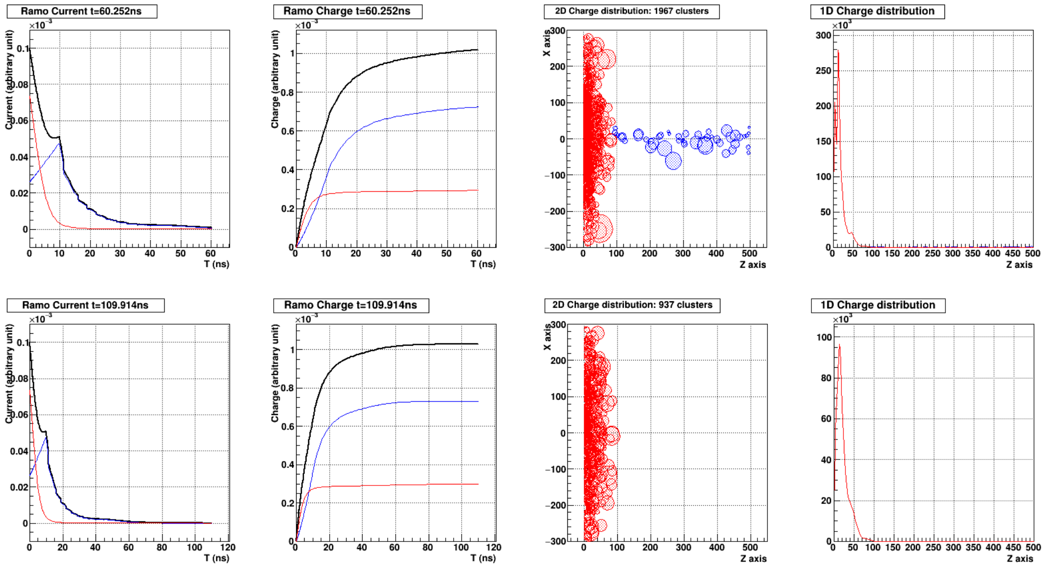

Figure 4.7: Collection process with 500-µm detector and 21.940 MeV α. The current and charge signals and the charge distribution are shown at several time instant (60 ns, and 110 ns) after the particle interaction. See Paragraph 4.2.1 for details.

4.2.2 Effects of the configuration parameters

Different signals can be obtained by simulating various particles and detectors. The particle properties, the detector configuration, and other simulation parameters affect the charge collection. Their effects are analyzed in the following.

The detector thickness influences the total amount of induced charge as described by the Ramo Theorem (Paragraph 2.3.4). The collection time generally increases by increasing the charge path. In the 147-µm, 500-µm and 1000-µm detectors, the signal rise-time varies from 43.5 ns to 30.6 ns and 121.3 ns in overdepleted configuration with 5.485 MeV α (Fig. 4.8). With the same incident particle, the thickness also impacts how the electron and hole motion contributes to the total signal.

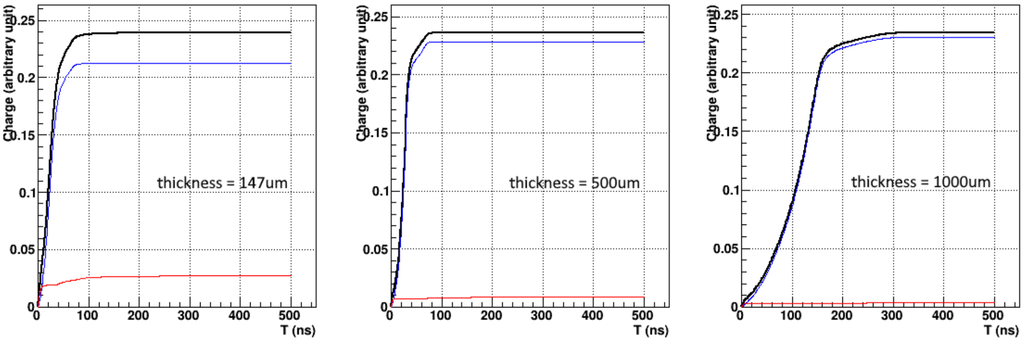

Figure 4.8: Example of simulated signals with 147-µm, 500-µm and 1000-µm detectors. The red and blue signals represent respectively the contribution of electron and hole motion to the induced charge. The bias voltage is bigger than the depletion one, but the internal electric is different in the three cases. Since the relative position of the ionization deposition decreses by increasing the detector thickness, the contribution of the holes to the total signal becomes predominant.

The macroscopic electric field is determined by the detector properties (2.18) and affects the charge velocity in the detector. The operating and depletion voltages of the device influence the collection process by changing the external field distribution along the silicon. Figure 4.9 shows the relation between the depletion voltage and the rise-time: as expected, in a detector with bias voltage near the depletion one, the signal rise-time increases since the charges in the low electric-field region move slower. In underdepleted configuration, the simulation may produce results with low accuracy (see Paragraph 2.3.6). Decreasing the bias voltage makes the rise-time increase since the bias electric field is lower.

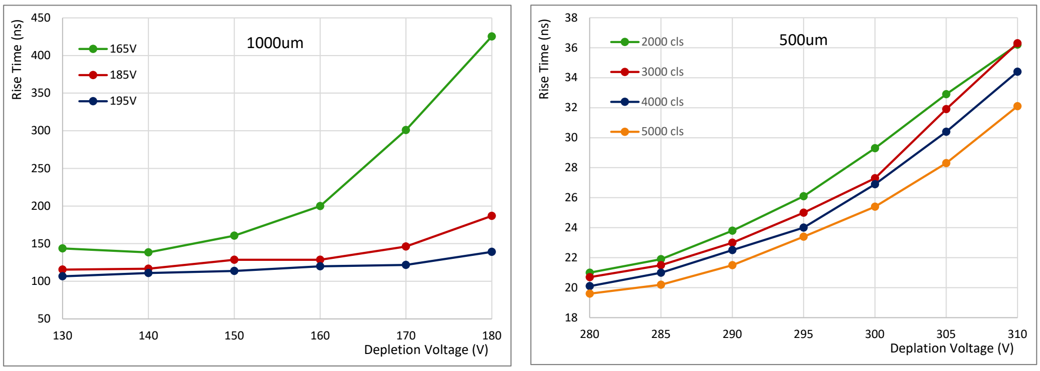

FIGURE 4.9: In the left graph, simulation of 5.485 MeV α with a 1000-µm detector (MICRO_FACTOR=1.5×10^{-6}, REDUCE_SQUASH=1 %, N_CLUSTERS=3000). Different bias voltages are shown (V_APPL=165 V,185 V,195 V). In the right graph, simulation of 21.940 MeV α with a 500-µm detector (MICRO_FACTOR=1.5×10^{-6}, REDUCE_SQUASH=1 %, N_CLUSTERS=3000, V_APPL=290 V).

Among the simulation free parameters, the MICRO_FACTOR is the most important. The inter-cluster interactions are a key aspect of the model, and the MICRO_FACTOR defines how the microscopic electric field is scaled compare to the macroscopic one. According to Figure 4.10, the rise-time is proportional to the MICRO_FACTOR since the Coulomb Forces between the clusters slow down the charge motion. It is also fundamental to the plasma erosion effect (Paragraph 2.3.5) and the column expansion inside the detector. Using a MICRO_FACTOR too large leads to the saturation of the charge velocity, and so the clusters would move in all directions since the bias field becomes negligible.

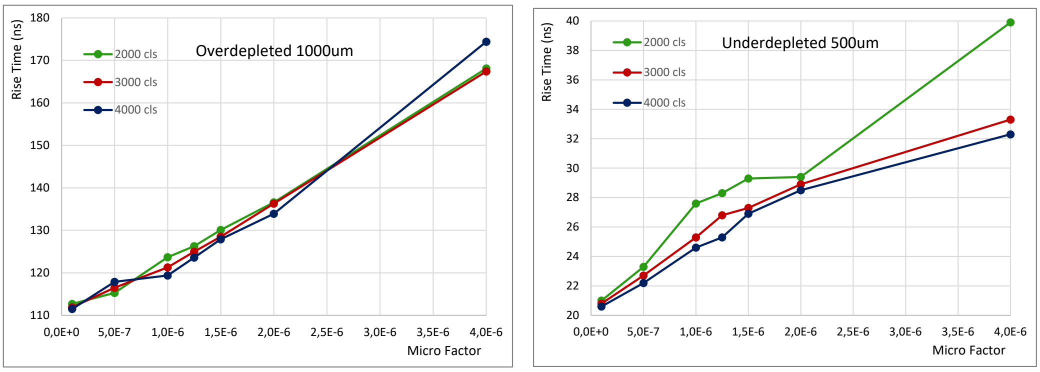

FIGURE 4.10: In the left graph, simulation of 5.485 MeV α with an overdepleted 1000-µm detector (REDUCE_SQUASH=1 %, V_APPL=185 V, V_DEPL=160 V). In the right graph, simulation of 21.940 MeV α with an underdepleted 500-µm detector (REDUCE_SQUASH=1 %, V_APPL=290 V, V_DEPL=300 V). In both graphs N_CLUSTERS=2000,3000,4000.

The REDUCE_SQUASH parameter slightly influences the total induced charge since the number of clusters involved is usually small. Using a REDUCE_SQUASH lower than 1 increases the simulation performance since the anomalous cluster charge is reduced (see Paragraph 3.1.5). The parameter is relevant in the first simulation phases, when lots of charges are generated near the collection electrodes and the detector is overdepleted, since it prevents charge peaks. In Fig. 4.11, an α is considered with both overdepleted and underdepleted devices.

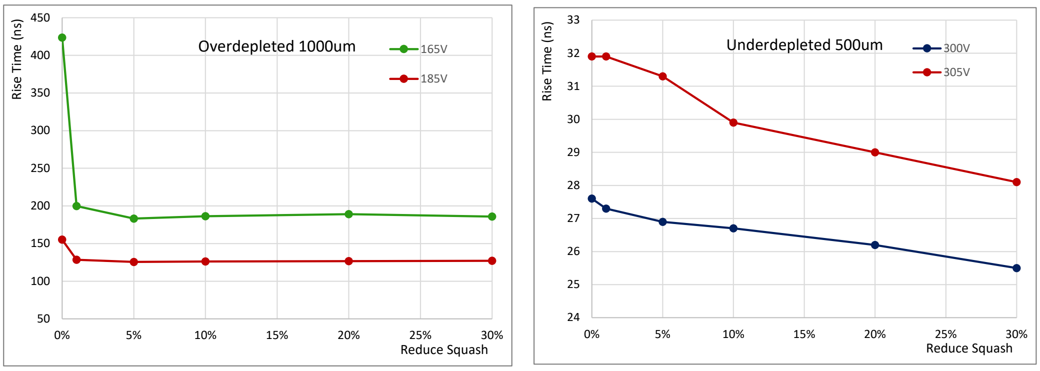

Figure 4.11: In the left graph, simulation of 5.485 MeV α with an overdepleted 1000-µm detector (MICRO_FACTOR=1.5×10^{-6}, V_APPL=165 V,185 V, V_DEPL=160 V). In the right graph, simulation of 21.940 MeV α with an underdepleted 500-µm detector (MICRO_FACTOR=1.5×10^{-6}, V_APPL=290 V, V_DEPL=300 V,305 V).

The total number of clusters is defined by NCLUSTERS_PER_MEV. Figure 4.12 and Figure 4.9(right) show the influence of the number of simulated clusters in case of respectively overdepleted and underdepleted detectors in case of α particles. The rise-time usually varies less than 2 ns with bias voltage higher than the depletion one. With devices near the depletion, the difference is below 5 ns.

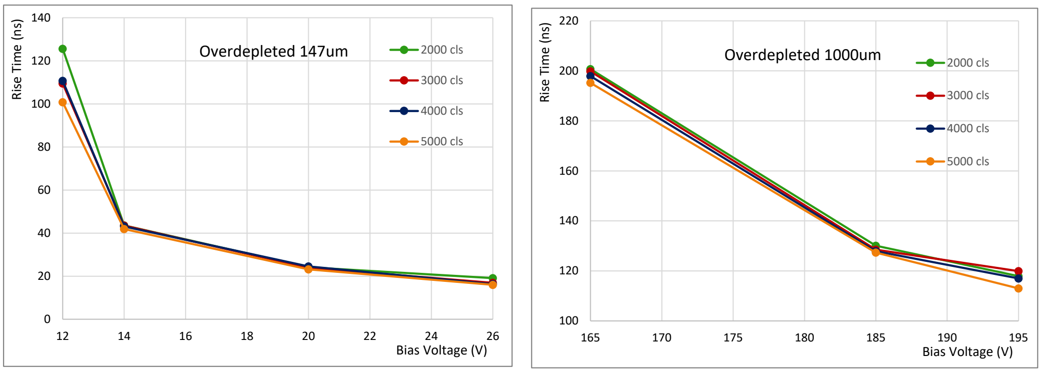

Figure 4.12: In the left graph, simulation of 5.485 MeV α with an overdepleted 147-µm detector (MICRO_FACTOR=1.5×10^{-6}, REDUCE_SQUASH=1 %, V_DEPL=12 V). In the right graph, simulation of 5.485 MeV α with an underdepleted 1000-µm detector (MICRO_FACTOR=1.5×10^{-6}, REDUCE_SQUASH=1 %, V_DEPL=160 V).

The atomic number Z and the atomic mass A affect the ionization charge distribution (see Paragraph 2.3.1) and, thus, the collection process. In Fig. 4.14(left), there are different particles with A=2Z+1 and almost the same energy-per-nucleon (~12 MeV/u): the relation between Z and rise-time is linear since the stopping power is proportional to Z^2/A, and the graph shows the effects of the number of simulated clusters on the collection time.

The ion energy determines the penetration depth that is one important factor to discriminate the incident particle. The Bragg peak position inside the detector influences the fraction of charge due to electron and hole motion, and the number of electron-hole pairs is proportional to the induced charge signal. Figure 4.13 shows the positive and negative charge contribution to the signal and the different rise-time with different energy ions. Figure 4.14(right) displays the relation between the incident ion energy and the max value of the output charge signal: as expected the correlation between the ion energy and the induced charge is linear and, thus, the comparison between the data can be performed by considering normalized signals (see Paragraph 3.2.3).

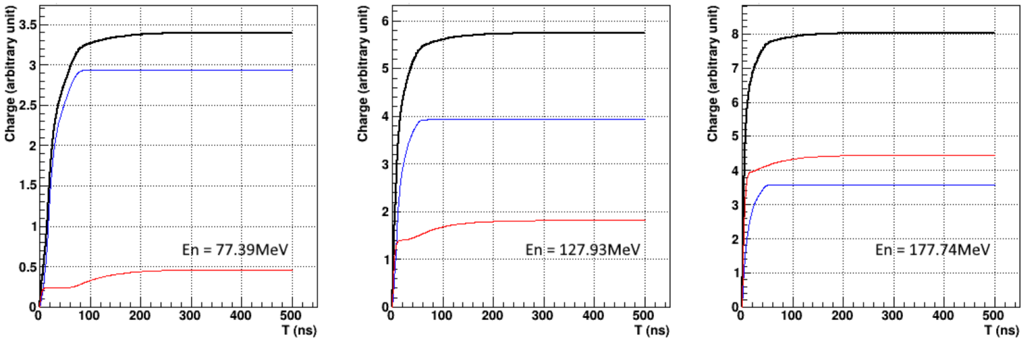

FIGURE 4.13: Example of simulated signals with 500-µm detector. In case of Z=6 (A=13), the particle energy determines the electron and holes contribution to the total induced charge since the penetration depth influences the average path length. The 77.39 MeV, 127.93 MeV, and 177.74 MeV particles enters the detector respectively ~115 µm, ~260 µm, and ~450 µm.

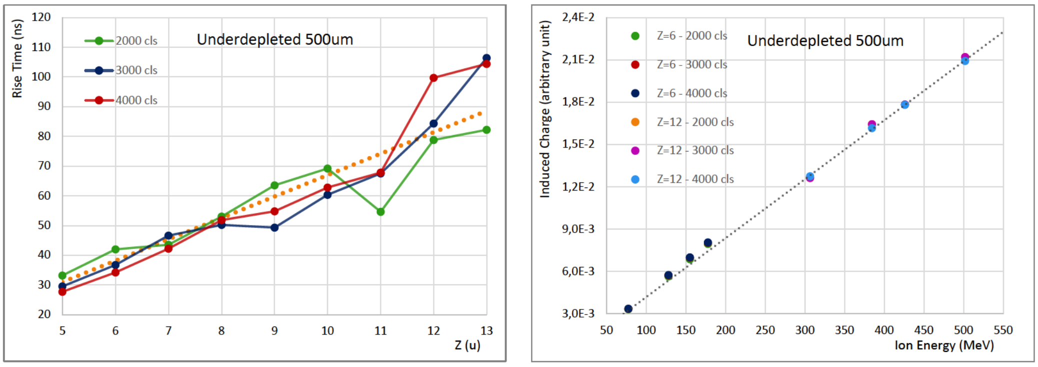

FIGURE 4.14: In the left graph, simulation of different particles with an underdepleted 500-µm detector (MICRO_FACTOR=1.5×10^{-6}, REDUCE_SQUASH=1 %, V_DEPL=300 V, V_APPL=290 V). The ion energy can vary between 11.5 MeV/u - 13.5 MeV/u. In the right graph, simulation of Z=6 (A=13) and Z=12 (A=26) with an underdepleted 500-µm detector (MICRO_FACTOR=1.5×10^{-6}, REDUCE_SQUASH=1 %, V_DEPL=300 V, V_APPL=290 V).

The particle energy affects the signal rise-time, as displayed in Fig. 4.15: increasing the energy makes the collection time decrease since a larger frantion of charges are generated in the high electric-field region, and the holes are nearer to the positive electrode. As it is also shown in Figure 4.14(left), the number of simulated clusters significantly influences the result when the initial energy is higher then ~300 MeV, and, thus, the total simulated charge is 13 µC (8.2×10^{13} electrons). Since the considered detector is underdepleted, the low-energy particle signal may have rise-time quicker than expected (see Paragraph 2.3.5).

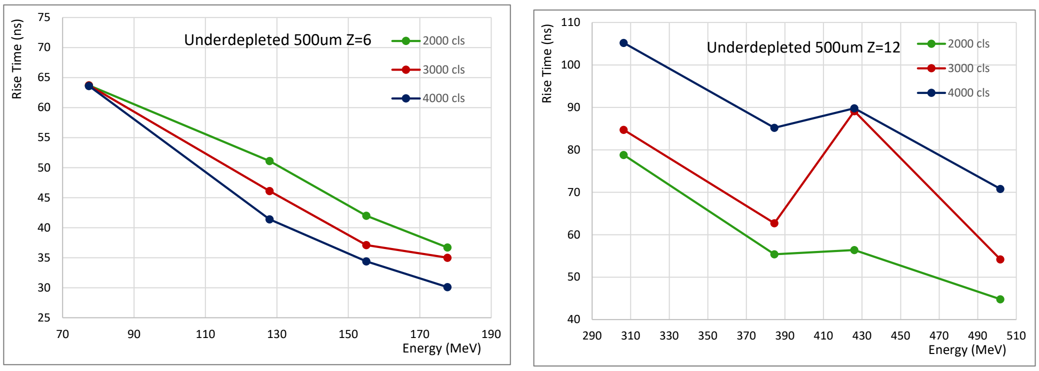

Figure 4.15: Simulation of Z=6 (A=13) and Z=12 (A=26) ion, respectively in left and right graph, with an underdepleted 500-µm detector (micro_factor=1.5×10^{-6}, reduce_squash=1 %, v_depl=300 V, v_appl=290 V).

4.2.3 Comparison with experimental signals

Regarding the EUCLIDES detectors, the results of the tested configurations are shown in Figure 4.16. With the 147-µm detector (left), the experimental data exhibits some oscillations due to the detector capacitance (see Paragraph 4.1.1). Nevertheless, there is a good match with the simulated signals: in all the three configurations (depletion voltage 12 V and bias voltage of 12 V, 14 V, and 20 V) the differences can be explained as effects of the acquisition chain. In the first case, where the oscillations are less relevant, the rise-time difference is 4.0 ns, and the MSE is −35.8 dB.
With the 1000-µm detector (right), the depletion voltage is estimated to be 150 V by evaluating the simulation results, and the experimental operating voltages are 165 V, 185 V, and 195 V. The considered depletion voltage is compatible with the experimental I-V characteristic (see Paragraph 4.1.1), and the simulated signals are in good matching with the experimental ones. In the three cases the Δtr is 195.5 ns, 33.6 ns, and 4.2 ns, and the MSE is −36.8 dB, −42.2 dB, and −42.7 dB. Especially in the first configuration, the rise-time of the simulated traces is very different from the experimental one, despite the simulation results seem quite good. The slow collection of the final electrons (Paragraph 4.2.1) generates long tails in the charge signals that are not present in the experimental data. That is probably due to the model that not considers the recombination processes (Paragraph 2.3.6) in the Silicon or the noise introduced by the motion of the inverse bias current charges (Paragraph 2.1.3) in the experimental data.

Figure 4.17 considers the FAZIA detector (Paragraph 4.1.2). With 21.940 MeV α (top-left), the simulation matches the experimental data with Δtr=0.3 ns and MSE=−38.3 dB. This particle have been simulated with various detector parameters to try to estimate both operating and depletion voltage, but the differences in the results are not sufficient to determine the precise value of both the unknown voltages. With bias voltage 290 V, the best results have been achived in a slightly underdepleted configuration with depletion voltage ∼300 V. In the other graphs the higher energy Z=6 particle is simulated with different energies (77.39 MeV, 127.93 MeV, and 177.74 MeV). If the particle stops in the middle of the detector (bottom-left), the simulation provides good results with rise-time difference of 1.8 ns and MSE of −41.7 dB. In case of larger energy and ion stop near the positive electrode, the simulated trace still fits the experimental one with MSE −37.1 dB, despite the simulated rise-time is 12.0 ns higher. With a lower energy particle (top-right), the collection process is quicker than expected since the simulated signal is very different to the experimental one (Δtr=57.7 ns and MSE=−31.1 dB).

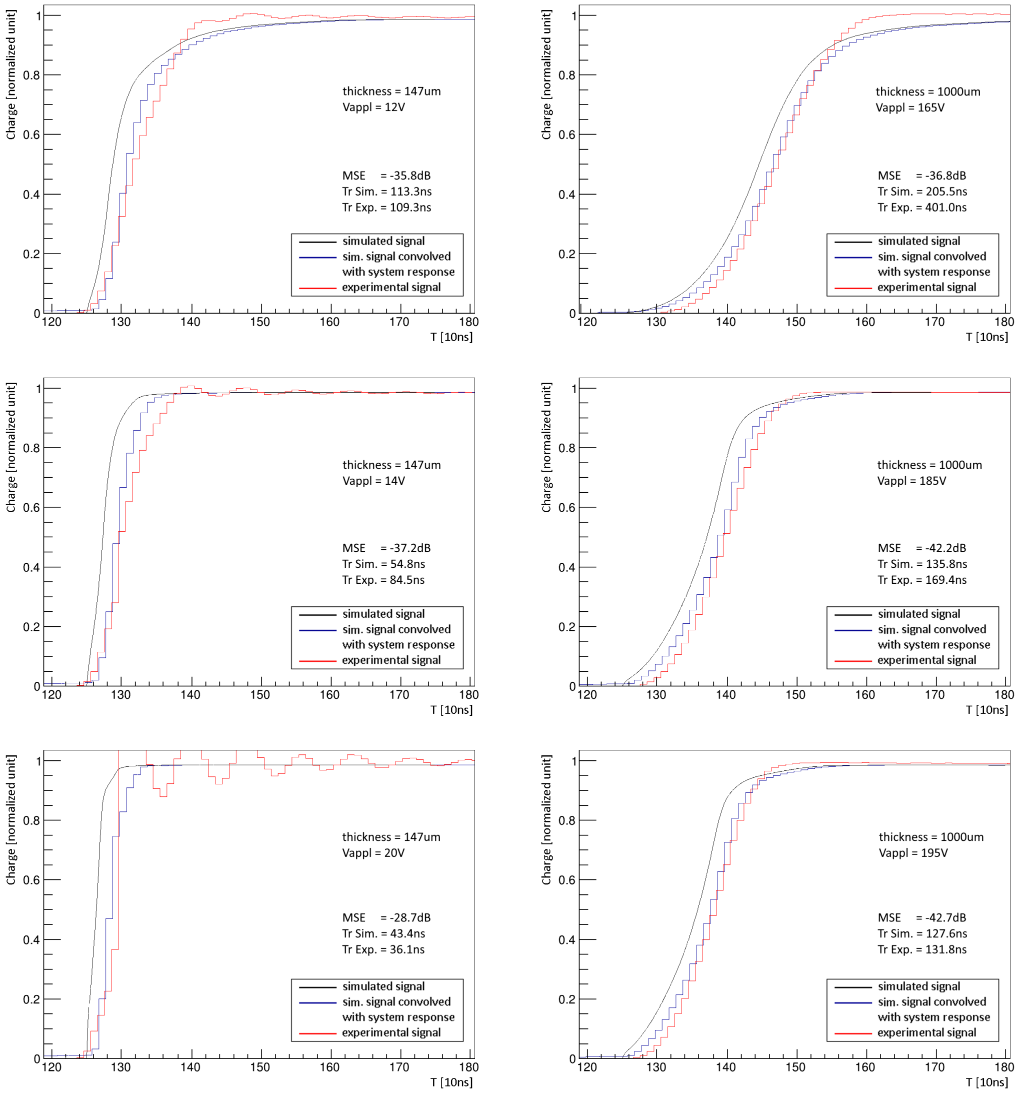

Figure 4.16: Comparison between experimental signals and simulated signals convoluted with acquisition chain response. On the left, simulation of 5.485 MeV α with 147-µm detector (MICRO_FACTOR=1.5×10^{-6}, REDUCE_SQUASH=1 %, N_CLUSTERS=3000, V_DEPL=12 V, V_APPL=12 V,14 V,20 V). On the right, simulation of 5.485 MeV α with 1000-µm detector (MICRO_FACTOR=1.5×10^{-6}, REDUCE_SQUASH=1 %, N_CLUSTERS=3000, V_DEPL=150 V, V_APPL=165 V,185 V,195 V).

The simulation has been performed with impinging energy up to 500 MeV and Z up to 13. In the following graphs, the average of the signals with a different number of clusters (from 2000 to 4000) is considered. In Figure 4.18 the pattern in the simulation behavior, shown with Z=6, is displayed with more particles. The graph on the left presents the MSE between simulated and experimental signals. As for the examples in Figure 4.17, MSE<-40 dB leads to an almost perfect match between the signals, while MSE<-37 dB points to signals with a high likelihood. The graph on the right shows the rise-time difference ($tr_{exp} - tr_{sim}$) between the signals. The Δtr is coerent since the simulated rise-time is longer with high-energy particles (that stop near the end of the detector) and shorter with low-energy particles (small penetration depth). This effect can be explained by a incorrect bias electric field, i.e. an imprecise estimation of the deplation or bias voltages of the detector. Since the device is underdepleted, the result is also influenced by the non-negligible charge diffusion due to a gradient of free charge concentration in the low electric-field region (Paragraph 2.3.6).

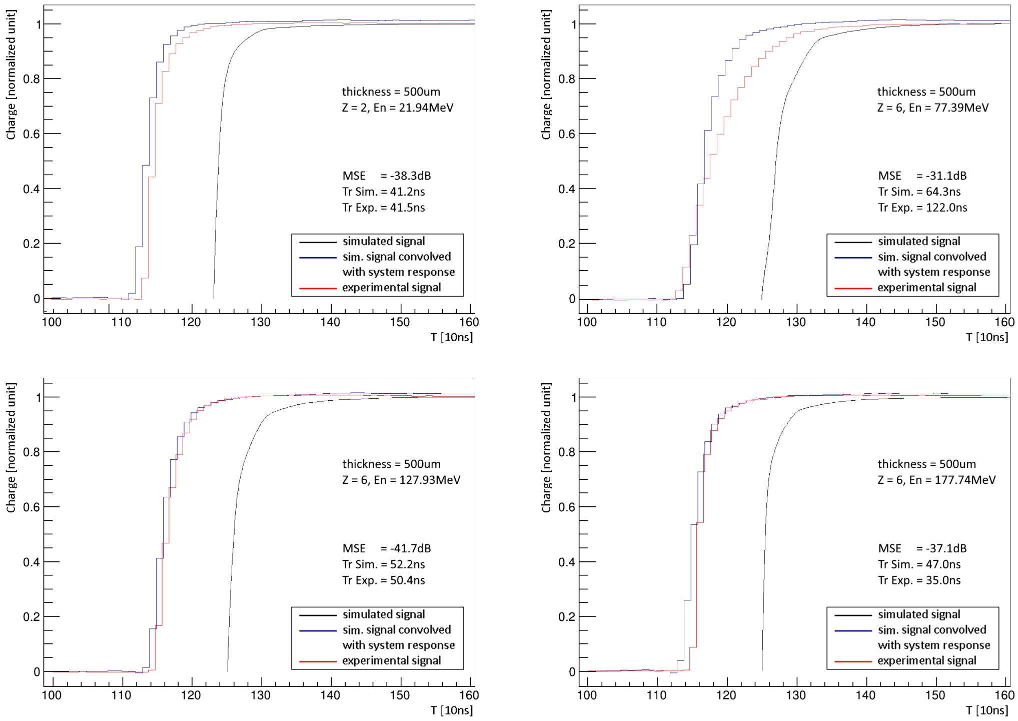

FIGURE 4.17: Comparison between experimental signals and simulated signals convoluted with acquisition chain response. Simulation of 21.940 MeV α (top-left), and Z=6 ion of 77.39 MeV (top-right), 127.93 MeV (bottom-left), and 177.74 MeV (bottom-right) with 500-µm detector (MICRO_FACTOR=1.5×10^{-6}, REDUCE_SQUASH=1 %, N_CLUSTERS=3000, V_DEPL=300 V, V_APPL=290 V).

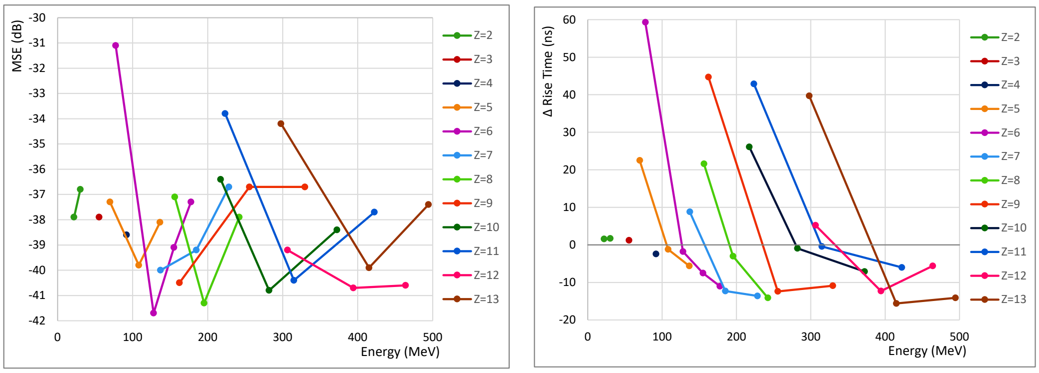

FIGURE 4.18: On the left graph, MSE between simulated and experimental signals. On the right graph, rise-time difference between the signals. The data are averaged over different simulation with 2000, 3000, and 4000 clusters (MICRO_FACTOR=1.5×10^{-6}, REDUCE_SQUASH=1 %, THICKNESS=500 µm, V_DEPL=300 V, V_APPL=290 V).

The correlation between the particle energy and the rise-time is important in the PSA since different ions belong to different loci (Fig. 4.19). The experimental signals in Figure 4.19(top) shows a big increment in the collection time with particles that stop near the entrance electrode since the device is underdepleted. This characteristic is not present in the simulated data in Figure 4.19(bottom) where the loci can still be identified and have a straight-line shape. This difference is partially explained in the discussion of Figure 4.18. As shown by the increasing size of the circles, the number of simulated clusters starts to influence the rise-time with higher energies and masses, and the simulation provides low-quality results.

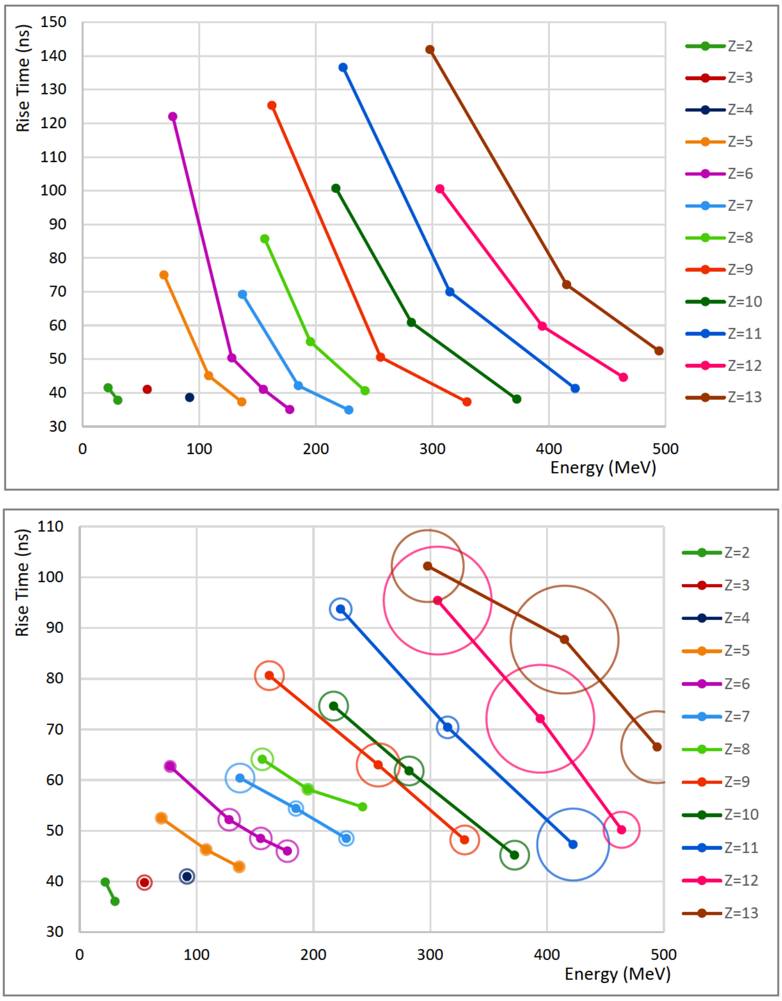

FIGURE 4.19: Correlation between particle energy and signal rise-time in case of different ions ($Z<14$) with a 500-µm underdepleted detector. The experimental (top) and simulated (bottom) signal particle loci are compared. The simulated data are averaged over different simulations, and the circles represent the accuracy in the rise-time by varying the number of simulated clusters between 2000 and 4000.

Conclusions and future developments 5

In this thesis, I have described the MicroSil model and compared it to the standard Drift-Diffusion approach. The main aspects of the model implementation have been discussed, and different configurations simulated and analyzed. The simulation results and the differences between simulated and experimental signals have then been evaluated considering the key parameters.
The model provides a good description of the charge collection process in silicon detectors, and the *cluster* approach makes the simulation able to handle a larger amount of charge compared to the TCAD, usually employed in electronic devices and circuits. The model has been tested with EUCLIDES and FAZIA detectors, and a dataset of various particles. The simulated signals are consistent with particles up to 300 MeV and up to Z=10 in a 500-µm detector. Particles that stop in the detector center seem to be simulated more accurately, in opposition to ions releasing a large amount of charge near the electrodes. The comparison between simulation results and experimental data shows a good matching for light ions in both overdepleted and slightly underdepleted detectors. However the results deteriorate with heavier particles and underdepleted devices.

Future developments will include experimental tests with other detectors, in particular overdepleted devices, and different particles. The model limits could also be improved by considering the free charge density in the silicon bulk and a more precise approximation of the cluster expansion mechanisms. In the future, the signal formation in both silicon strip and pad detectors, where the Ramo's weight field is more complex, is expected to be implemented.

Bibliography

[1] Vito Manzani. Lecture 2. semiconductor detectors, signal, noise and electronics. 2015. URL `https://indico.cern.ch/event/453690/sessions/99350/`.

[2] Glenn F. Knoll. *Radiation Detection and Measurement, 3rd ed.* John Wiley and Sons, 3rd edition edition, 2000.

[3] Ansgar Jüngel. *Transport Equations for Semiconductors.* Springer Berlin Heidelberg, 2009.

[4] S E Guidoni and C M Aldao. On diffusion, drift and the einstein relation. *European Journal of Physics*, 23(4):395–402, jun 2002. doi: 10.1088/0143-0807/23/4/302.

[5] E. J. Schioppa, J. Idarraga, M. van Beuzekom, J. Visser, E. Koffeman, E. Heijne, K. J. Engel, and J. Uher. Study of charge diffusion in a silicon detector using an energy sensitive pixel readout chip. *IEEE Transactions on Nuclear Science*, 62(5):2349–2359, 2015. doi: 10.1109/TNS.2015.2475124.

[6] Nandha Kumar Subramani. *Physics-based TCAD device simulations and measurements of GaN HEMT technology for RF power amplifier applications.* PhD thesis, 2017. URL `https://tel.archives-ouvertes.fr/tel-01702325`.

[7] Synopsys tcad. URL `https://www.synopsys.com/silicon/tcad.html`.

[8] $sentaurus^{TM}$ device user guide. URL `https://www.researchgate.net/profile/Nabil-Ashraf/post/How-to-control-the-slope-of-output-characteristicsId-Vd-of-a-GAA-nanowire-FET-which-shows-flat-saturated-region/attachment/5de3c15bcfe4a777d4f64432/AS%3A831293646458882%401575207258619/download/Synopsis_Sentaurus_user_manual.pdf`.

[9] Pablo Fernández Martínez. Simulation of seb with sentaurus tcad. 2017. URL `https://indico.cern.ch/event/637708/contributions/2583381/`.

[10] Franck Nallet. Sentaurus tcad introduction. 2014. URL `https://idpasc.lip.pt/uploads/talk/file/106/TCAD_intro_2014.pdf`.

[11] Luigi Bardelli. *Development of sampling and digital signal processing techniques with applications to Nuclear Physics detectors.* PhD thesis, 2005.

[12] Luigi Bardelli and Giacomo Poggi. Simulation and study of current signals and plasma effects in silicon detectors for heavy ions experiments, 2005.

[13] F. Hubert, R. Bimbot, and H. Gauvin. Semi-empirical formulae for heavy ion stopping powers in solids in the intermediate energy range. *Nuclear Instruments and Methods in Physics Research Section B: Beam Interactions with Materials and Atoms*, 36(4):357 – 363, 1989. doi: 10.1016/0168-583X(89)90339-X. URL `http://www.sciencedirect.com/science/article/pii/0168583X8990339X`.

[14] D. Schwalm, E.K. Warburton, and J.W. Olness. Coulomb excitation of sd shell nuclei: A self-contained set of b(e2) values and lifetime measurements. *Nuclear Physics A*, 293(3): 425 – 480, 1977. doi: 10.1016/0375-9474(77)90108-7. URL `http://www.sciencedirect.com/science/article/pii/0375947477901087`.

[15] Simon Ramo. Currents induced by electron motion. *Proc. Ire.*, 27:584–585, 1939. doi: 10.1109/JRPROC.1939.228757.

[16] Bernette Kolbinger. Simulation of a silicon-strip detector, 2012. URL `http://personalpages.to.infn.it/~cartigli/Weightfield2/Manual_files/Manual_Weightfield.pdf`.

[17] Root: Data analysis framework. URL `https://root.cern/`.

[18] Mark E. Davis. *Numerical methods and modeling for chemical engineers*. Wiley, 1984.

[19] Gsl - gnu scientific library. URL `https://www.gnu.org/software/gsl/`.

[20] C. William Gear. *Numerical Initial Value Problems in Ordinary Differential Equations*. Prentice Hall PTR, USA, 1971.

[21] Leslie Greengard. *The rapid evaluation of potential fields in particle systems*. MIT press, 1988.

[22] Gunnar Martinsson. Lecture 2: The fast multipole method. 2014. URL `https://amath.colorado.edu/faculty/martinss/2014_CBMS/Lectures/lecture02.pdf`.

[23] Pierre Gay. Aran, une librairie pour la méthode des multipôles. 2014.

[24] Libaran, a 2d/3d fast multipole method software library. URL `https://github.com/pigay/aran`.

[25] Donald Meagher. Octree encoding: A new technique for the representation, manipulation and display of arbitrary 3-d objects by computer. Technical report, 1980.

[26] Pierre Gay. La librairie aran : parallélisation de la méthode des multipôles rapides en mémoire distribuée. 2014. doi: 10.13140/2.1.2312.7840.

[27] D. Testov, D. Mengoni, Alain Goasduff, A. Gadea, R. Isocrate, Philipp R. John, D. Bazzacco, Ciro Boiano, A. Boso, P. Cocconi, J.A. Dueñas, F.J. Egea, L. Grassi, Katarzyna Hadyńska-Klęk, Grzegorz Jaworski, S. Lunardi, R. Menegazzo, D. Napoli, and J. Valiente-Dobón. The 4π highly-efficient light-charged-particle detector euclides, installed at the galileo array for in-beam γ-ray spectroscopy. *The European Physical Journal A*, 55, 04 2019. doi: 10.1140/epja/i2019-12714-6.

[28] S. Barlini, Manny Bini, Antonio Buccola, Alberto Camaiani, Giovanni Casini, Caterina Ciampi, Catalin Frosin, Pietro Ottanelli, G Pasquali, Silvia Piantelli, G Poggi, A. Stefanini, S Valdré, E Bonnet, Bernard Borderie, Remi Bougault, A Chibli, Magda Cicerchia, Marco Cinausero, and M Vigilante. Fazia: a new performing detector for charged particles. *Journal of Physics: Conference Series*, 1561:012003, 06 2020. doi: 10.1088/1742-6596/1561/1/012003.

[29] Ciro Boiano, Roberto Bassini, Alberto Pullia, and Angelo Pagano. Wide-dynamic-range fast preamplifier for pulse shape analysis of signals from high-capacitance detectors. *Nuclear Science, IEEE Transactions on*, 51:1931 – 1935, 11 2004. doi: 10.1109/TNS.2004.832308.